Laser induced vibrational excitation of acrylonitrile adsorbed on copper

Robert Wallauer

Diplomarbeit
am Institut für Kernphysik
der Johann-Wolfgang-Goethe-Universität
Frankfurt am Main

und

Instituto Plurisdisciplinar
Unidad de Laséres y Haces Moleculares
Universidad Complutense
Madrid/Spain

09. Mai 2006

Ich versichere hiermit, dass ich die vorliegende Arbeit selbständig verfasst, keine anderen als die angegebenen Hilfsmittel verwendet und sämtliche Stellen, die benutzten Werken im Wortlaut oder dem Sinne nach entnommen sind, mit Quellen- bzw. Herkunftsangaben kenntlich gemacht habe.

Frankfurt am Main, den 4. April 2006

Meiner Familie und Dani

Contents

1. Introduction

In a collision processes of electrons with molecules, the difference between the masses of the nucleus and the electron makes the process of energy transfer (e.g. vibrational excitation) seem rather unlikely.

If however the electron is attached by the molecule to create a negative ion, the collision time increases so that the energy transfer between both is much more probable. This process, which has been discovered in the 70s is called resonant vibrational excitation and its behavior is well known in gas phase [1]:

$$e^- + AB(\nu_i) \rightarrow AB^{-*} \rightarrow AB^*(\nu_i) + e^- \tag{1.1}$$

It is characterized by cross sections of great excitation, well known kinetic energy ranges of the incident electrons and angular distribution of the scattered electron as a product of the negative ion symmetry.

This process has been observed also in molecules adsorbed on surfaces [2], but many aspects are still unknown due to its complexity. In general the resonances of vibrational excitation of molecules adsorbed on surfaces are by collision of low kinetic energy electrons in the energy range between 0 and 5 eV. For physisorbed molecules on metals, the influence of the surface on the molecule is very weak, so that the expected resonances are similar to those in gas phase. The situation for the chemisorbed molecules is more complex, given that the adsorption induces changes in the electronic structure of the molecule, even enabling charge transfer between both.

Electron-driven molecular processes have obtained increasing attention in the last years, also due to several european networks like *RADAM* (Radiation damage in biomolecular systems) or *EIPAM* (Electron-induced processing at

the molecular level), in which collision of low energy electrons with molecules adsorbed on surfaces or in gas phase are studied. The aim is to control reactions in which low energy free electrons, tunneling electrons, or photoelectrons at surfaces or in the condensed phase play a key role in either starting reactions or in guiding their evolution [3]. Control of the electron energy, flux, and coherence allows the exploration of alternative reaction pathways and products as those that would be obtained by thermal chemistry.

The electrons which interact with the molecule can be created, for example, with an electron monochromator [4] or by photons that create an electron beam from the surface. The application of laser radiation to generate electronic emission from solids started just at the beginning of the development of laser beams in 1960 [5]. First laser induced electron emission from metals has been identified as thermal emission in 1965 by Ready[6]. It took until the late 60s to discover the photoemission from metals and beginning 70s to characterize photoemission processes where the photon energy is lower than the work function so that the process must be a multiphoton ionisation.

The crucial parameter in the multiphoton emission is the laser pulse duration since the absorbed energy of the electrons can be redistributed before the ejection of the electron to the vacuum by electron-electron or electron-phonon scattering. The relaxation times in dense materials like metals are extremely short, in the order of femtoseconds (10^{-15} s) for the electron-electron scattering and picoseconds (10^{-12} s) for the electron-phonon scattering [7]. Therefore as Logothetis and Hartmann [8] point out nanosecond laser pulses can generate photocurrents in metals always influenced by thermal effects that can not be ruled out.

A great progress has been achieved with the emergence of ultra-short laser pulses. They open the possibility of non-thermal reactions on surfaces since the electrons are not in thermal equilibrium with the surface. In this case different reaction pathways are possible depending on the pulse duration [9, 10]. In a thermal induced reaction the thermodynamical equilibrium lasts much longer than the characteristic time-scale of a molecular vibration, so that the reaction will take place along those coordinates having the lowest activation barrier.

But not only pulse duration plays a significant role in the reaction pathway but also the wavelength, especially in the Infrared [11, 12, 10], since most of the vibrational excitation modes are located at these energies. In 2000 [13, 14] catalytic processes of acrylonitrile on copper have been observed by the Madrid group in which non-thermal effects play a role even though the

photoelectrons are in thermal equilibrium with the surface. Nevertheless an enhancement in the process

$$ACN(ads) + e^- \rightarrow CN^-(gas) + A(ad\,org) \tag{1.2}$$

has been observed. This reaction was considered to be either *Substrate-mediated* (thermal) or *Adsorbate-mediated* (vibrational absorption by the molecule).

Since the thermal effects in this measurements played a major role, a new experiment has been set up in the Unidad de Láseres y Haces Moleculares to study the vibrational excitation of the molecule by photoelectron spectroscopy with shorter laser pulses (nano- and femtosecond). For the observation of the reaction products a new time of flight mass spectrometer (TOF-MS) had to be designed. With this TOF-MS not only ions could be detected but also the kinetic energy of electrons measured with less resolution than in an electrostatic electron analyzer but with a higher efficiency.

This document is diveded into three parts. First part (chapter two) gives a short introduction of the physical and chemical principles, starting with the theory of photoemission, describing the adsorbation process of molecules on surfaces and the photochemical reaction of acrylonitrile on copper. Second part (chapter two) describes the experimental setup used for this work and the design process of the TOF-MS. In the last part (chapter four and five) the results obtained in the experiment are discussed and a short outlook is given.

2. Physical Principles

2.1 Photoemission from surfaces

The phenomenon of photoemission was detected by Hertz [15] in 1887. He found that the kinetic energy of the emitted electrons was not depending on the light intensity but on the frequency. Its explanation took until 1905 when Einstein published his famous paper about the quantum nature of the light [16]. He proposed that electrons ejected from a solid have the kinetic energy of the incident photon minus the energy needed to overcome a body-specific barrier:

$$E_{kin} = h\,\nu - \phi \tag{2.1}$$

In this description only electrons near the surface are taken into account. It is called *surface photoelectric effect* due to emission of free electrons from the conduction band while they are interacting with the surface barrier. In principle also the *volume photoelectric effect* has to be considered, which is emission of the bound electrons in the crystal in which the photons need an additional energy to overcome the binding energy of the electrons.

This concept is shown in figure 2.1. The hatched area represents the density of states (DOS) near the surface of the outermost band. Divided by a large energy gap are the core levels of the crystal atoms. Since all the binding energies are with respect to the Fermi energy the work function (i.e. the gap between Fermi level and vacuum level) has to be subtracted from the final kinetic energy of the electrons.

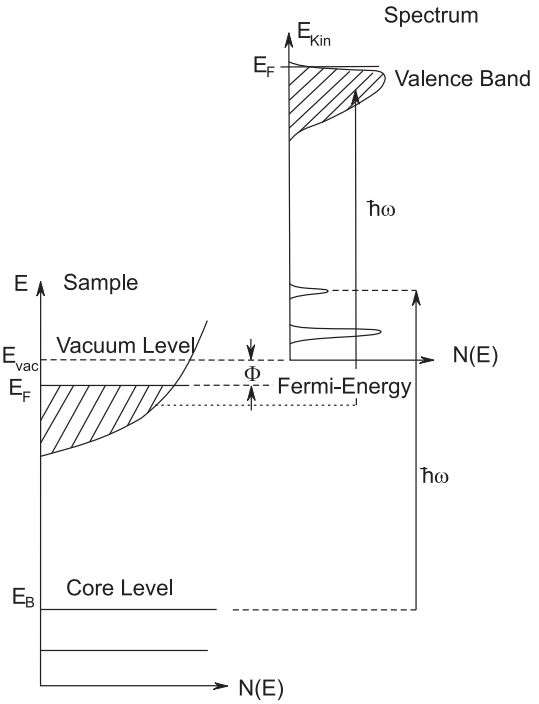

Figure 2.1: The concept of Photoelectron spectroscopy, taken from [17]. The hatched area represents the density of states near the Fermi energy.

2.1.1 Theoretical concepts of photoemission

The most commonly used model for the interpretation of photoemission is the so-called "Three-Step-Process" developed by Berglund and Spicer [18] in which the photoemission process is subdivided into optical excitation, transport to the surface and emission.

In this model the excitation process is described by a transition from an initial state ($|\psi_i\rangle$) characterized by energy and wave vector to a final state ($|\psi_f\rangle$). The probability $w_{i->f}$ is given by Fermi's Golden Rule

$$w_{i->f} = \frac{2\pi}{\hbar}|\langle\psi_f|H_{WW}|\psi_i\rangle|^2\rho(E) \tag{2.2}$$

so that the transition probability depends on the matrix element of the perturbation H_{WW}. In the transport process to the surface the electrons are scattered elastically and inelastically. The loss of electrons can be calculated in this picture by the mean free path $\lambda(E,k)$ in which the impact frequency parameter τ is a function of the energy

$$\lambda(E,k) = \frac{\tau}{\hbar}\frac{dE}{dk} \tag{2.3}$$

so that the fraction of electrons reaching the surface is given by

$$d(E,k) = \frac{\alpha\lambda}{1+\alpha\lambda} \tag{2.4}$$

where λ is the absorption coefficient of the material. The transition of the electrons into the vacuum can be described analog to the refraction of a light beam at the transition between two optical media (Snellius law). The electrons have to overcome the potential barrier $V = E_{Fermi} + \Phi = E_{vac} - E_0$, where E_0 is the lower end of the valence band, which means that the kinetic energy parallel to the surface normal has to be equal or larger.

$$\frac{\hbar}{2m}K_{\parallel}^2 \geq E_{vac} - E_0 \tag{2.5}$$

Electrons with an energy lower than the surface barrier will be reflected back into the crystal. It has to be pointed out that in this model the surface barrier affects only the parallel momentum vector and as a result the angle of emission ϑ (relative to the surface normal) of the electron with wavevector $p/\hbar$ relative to ϑ' with K' into the crystal is changed.

$$p_{\parallel}/\hbar = sin\,\vartheta\sqrt{\frac{2m}{\hbar^2}E_f - E_0} = sin\,\vartheta'\sqrt{\frac{2m}{\hbar^2}E_f - E_{vac}} = K'_{\parallel} \tag{2.6}$$

From this a critical angle can be calculated below which the escape from the crystal is not possible for the electrons:

$$sin\,\vartheta_{crit} = \sqrt{\frac{E_f - E_{vac}}{E_f - E_0}} \tag{2.7}$$

Since the angle $0 \leq \vartheta \leq \vartheta_{crit}$ describes a cone for which emission to the vacuum is possible it is called the *escape cone*.

The Three-Step-Model includes several inaccuracies, like the missing consideration of interference of bulk- and surface-states or a too simplified barrier model. Therefore a more rigorous treatment has been developed by Pendry in a *One-Step-Model* [19]. The whole process of photoemission is seen as a scattering process in which an incident optical wave creates an electron wave from the bulk. Starting point is again Fermi's Golden Rule (eq. 2.2), where the excitation is not into a bulk state but into a damped state which has to be fit to a plain wave outside the bulk. In this way scattering and surface effects can be considered without the wave coherence in the different stages of the process.

2.1.2 Work function

To describe the potential distribution electrons see near the surface, the periodic volume potential into the crystal can not be cut off at the surface atom and continued constant into the vacuum. The electrons need additional energy to be ejected to the vacuum level. This potential barrier has several reasons.

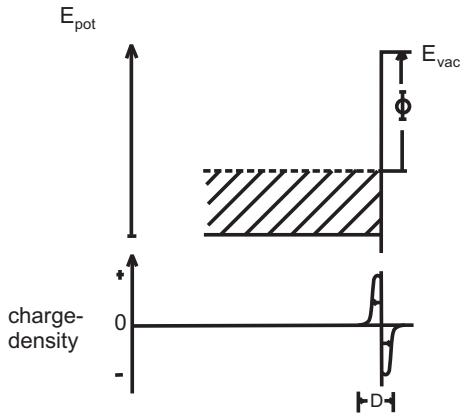

Figure 2.2: Work function and Debye lenght.

The volume states at the surface differ in density and therefore in charge from the states of the substrate, so that the surface has a surface charge which is compensated by charges in the substrate. The thickness of the resulting dipole layer is determined by the density of free charges in the volume. The perturbation range of electric fields due to charge separation at the surface is called *Debye-length* (fig. 2.2).

Another contribution to the potential barrier comes from the many-body interaction of the valence electrons between each other and the interaction of valence electrons with inner-shell electrons.

The work function is easier accessible in experiments than the surface potential barrier and therefore it is used for characterization of materials. It is defined by the energy difference between two states of equilibrium, one of N electrons in the crystal and another of $N-1$ electrons in the crystal and one electron with zero kinetic energy far away from the surface. With this definition the work function can be written as [20]

$$\phi = E_{vac} - (E_N - E_{N-1}) = E_{vac} - E_F \tag{2.8}$$

which is simply the difference between the Fermi-energy and the vacuum level (fig. 2.2).

Since the Fermi-energy is defined at 0 K as the energy of the highest occupied state, for higher temperatures electrons can occupy states higher than the Fermi-energy, following the Fermi-Dirac distribution, and can be ejected with less energy than the work function.

2.1.3 Temperature dependence of photoemission

For the high power densities applied by laser light the influence of the laser irradiation on the surface cannot be neglected.

The process of heating is carried out by relaxation of electrons, previously excited by laser irradiation. The excitation rapidly decays into heat ($10^{-12}s$) [21]. The heat diffuses with time t during the laser pulse a distance $d = \sqrt{2\kappa t}$ into the solid (thermal diffusion length), where κ is the thermal diffusivity. The temperature rise of a laser-heated surface can be calculated from the heat conduction equation with the laser treated as a surface heat source and the heat flow is considered to be one-dimensional into the solid. The surface temperature rise is than given by [22]:

$$\triangle T(t) = \frac{F_0}{K}\sqrt{\frac{\kappa}{\pi}}\int_0^t A(t-\tau)\sqrt{\tau}d\tau \tag{2.9}$$

where $A(t)$ is the normalized temporal profile of the laser pulse, F_0 the density of maximal absorbed power , K the thermal conductivity (3.85 W cm^{-1} K^{-1} for copper), κ the the thermal diffusivity (1.12 cm^2/s).

The first theory to successfully explain both the temperature dependence of one-photon photoemission and the spectral dependence of one-photon photoemission near the work-function was developed by Fowler [23]. Fowler's starting point is the assumption that the electrons in the metal obey Fermi-Dirac statistics and are uniformly distributed in momentum space. He calculated the one-photon quantum yield for three different models that depend on how the photon was absorbed and the electron escaped. Shortly thereafter DuBridge [24] extended Fowler's calculations using slightly different assumptions for both the absorption and the electron emission, and he calculated the one-photon quantum yield as a function of temperature and one-photon energy.

These ideas of Fowler and DuBridge were extended to more general electron emission effects by Bechtel [25]. The basic tenet is that the total current

density is composed of partial current densities each of which has a simple interpretation. Thus the total current density can be written as:

$$\vec{J}(\vec{r},t) = \sum_{n=0}^{\infty} \vec{J}_n(\vec{r},t) \tag{2.10}$$

where J_0 is interpreted as thermionic emission, J_1 as one-photon photoemission, and J_n as n-photon photoemission. The result for the n-photon current density is

$$|\vec{J}_n(\vec{r},t)| = a_n(e/h\nu)^n AI(\vec{r},t)^n(1-R)^n T(\vec{r},t)^2 F\left(\frac{nh\nu-\phi}{KT(\vec{r},t}\right) \tag{2.11}$$

where e is the electron charge, R the surface reflectivity, A is the theoretical Richardson coefficient, $h\nu$ is the laser photon energy, ϕ is the surface work function, K is Boltzmann's constant, I is the incident laser irradiance, T is absolute temperature of the surface and a_n is a constant. The function $F(x)$ is the Fowler function.

2.1.4 Polarization of the incident light

It has been shown in various experiments [26, 27], that the photoemission is highly dependent not only on the angle of incidence but also on the polarization. It can be subdivided into two independent polarizations (figure 2.3), one with the electric field vector parallel to the plane of incidence (p-polarization) and the other perpendicular to it (s-polarization).

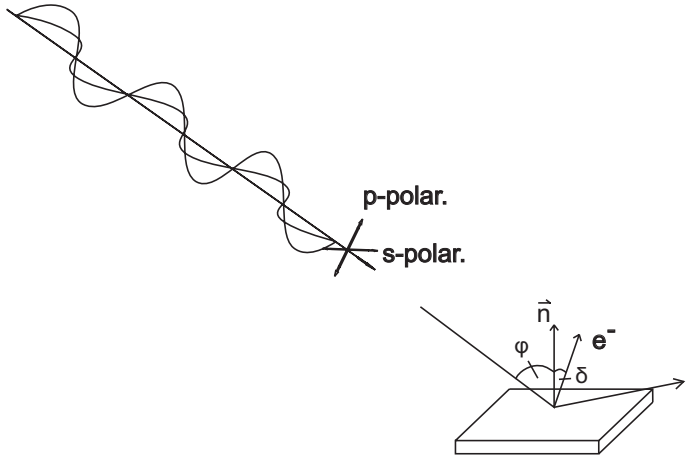

Figure 2.3: Polarization of the incident light and relevant angles in the photoemission process, φ giving the angle of incidence and δ giving the angle of the emitted electrons both in relation to the surface normal.

The incoming and the reflected wave form a standing wave at the boundary. In the case of an absorbing material this wave stretches into the bulk. For

s-polarization only a component parallel to the surface can exist, whereas for p-polarization two components are present: one in the plane of the surface and one parallel to the surface normal. The Fresnel equations give the ratio of reflected and refracted light

$$r_s = \frac{cos^2\theta - \sqrt{n_2^2 - sin^2\theta}}{cos^2\theta + \sqrt{n_2^2 - sin^2\theta}} \tag{2.12}$$

$$r_p = \frac{n_2^2 cos^2\theta - \sqrt{n_2^2 - sin^2\theta}}{n_2^2 cos^2\theta + \sqrt{n_2^2 - sin^2\theta}} \tag{2.13}$$

where n_2 is the refractive index of the material and θ the angle between material plane and incoming beam. The reflectivity at the boundary is then given by

$$R_{s,p} = |r_{s,p}|^2 \tag{2.14}$$

Concerning the electron yield, theory of photoemission states that it is entirely dependent on the bulk absorption coefficient, which can be written in the nonlinear case as $(1 - R)^n$, where n is the nonlinearity order. The ratio between s- and p-polarization can then be written as

$$\frac{Y_p}{Y_s} = \frac{(1 - R_p)^n}{(1 - R_s)} \tag{2.15}$$

By measuring the desorption yield of a molecule from a metal surface for both polarizations and comparing them with the theory it can be demonstrated that absorption by the metal rather than direct absorption by the molecule is the dominant process.

2.2 Adsorption on metals

Adsorption of molecules on surfaces can be subdivided into physical adsorption, or *physisorption* and chemical adsorption, *chemisorption*. Physisorption is characterized by a lack of a true chemical bond between the adsorbate and the substrate. The attractive force is the van-der-Waals interaction.

In Chemisorption the molecular electrons overlap with the valence or conduction electrons at the planar surface, so that for a qualitative approach the same theoretical methods can be used as in the theory of chemical bonding.

In a simplified model, one can consider an adsorption system of a molecule with a partially-filled molecular orbital M and a transition metal with a partially-filled d-band. The orbital overlap between M and d lead to chemisorption with rehybridisation and the formation of new Md orbitals. In

this description the d-band is represented by a single energy level and interactions with the s- and p-states and with molecular orbitals other than M are neglected. An approximate wave function for the adsorbate-metal system may be formulated as [28]

$$\psi = a\,\psi_1(M^-, d^\circ+) * b\,\psi_2(M^+, d^-) \tag{2.16}$$

where ψ_1 and ψ_2 represent *charge-transfer states*. ψ_1 describes a state in which an electron is transferred from the metal state into the molecular orbital, whereas ψ_2 refers to the reverse situation. The calculation of the new chemisorption energy levels is performed by minimizing the energy functional [28]

$$E = \frac{\langle\psi|H|\psi\rangle}{\langle\psi|\psi\rangle} \tag{2.17}$$

where H is the total Hamiltonian of the system (molecule plus substrate).

For a more accurate description of the chemisorption bond the wave function $\psi_0(M, met)$ of the no-bond state (separated substrate (met) and molecule (M)) and charge transfer into all unoccupied Bloch states ($k > k_F$, k_F: Fermi wave vector) and from all filled metal states ($k < K_F$) into the molecular orbital have to be taken into account. Instead of (2.16) one uses [30]

$$\psi = N\,\psi_0(M, met) + \sum_{k<k_F} a_k\,\psi_k(M^-, met^+) + \sum_{k>k_F} b_k\,\psi_k(M^+, met^-) \tag{2.18}$$

to minimize the energy functional (2.17).

As in the orbital theory of molecular bonding, the concept of "frontier orbitals" is also useful in a description of chemisorption bonds. The strongest interaction with the adsorbing molecule occurs for an overlap between occupied and unoccupied, i.e. by electron transfer into the Lowest Unoccupied Molecular Orbital (LUMO) and by electron donation from the Highest Occupied Molecular Orbital (HOMO) into an empty substrate state. Carrying out the minimization procedure of (2.17) by means of (2.18) leads to [30]

$$E_b - E_{nb} = \sum_{k<k_f} \frac{|U_{Lk}|^2}{E_k - E_{LUMO}} + \sum_{k>k_f} \frac{|U_{Hk}|^2}{E_{HOMO} - E_k} \tag{2.19}$$

for the total energy difference between the bonding (E_b) and the non-bonding state (E_{nb}). E_k are the energies of the unperturbed metal Bloch states (or possibly surface states involved in the bonding), E_{LUMO} and E_{HOMO} are the unperturbed molecular orbital energies, whilst U_{Lk} and U_{Hk} are interaction

matrix elements between the metal orbital k and the LUMO ($k < k_F$) and the HOMO ($k > k_F$), respectively.

2.2.1 Adsorbate-induced changes in the work function

In the case of strong chemisorption charge is shifted from the molecule to the substrate and vice versa, thus giving rise to additional dipoles, whose fields act on the emitted electrons. These effects lead to a change in the work function $\triangle\phi$.

The dipole contribution of a monolayer on an adsorbate is often calculated on a simple model in which the dipole-induced work function change is described in terms of the emitted electrons crossing a parallel plate capacitor of plate separation d. The total charge density is $n_{dip}\, q$, n_{dip} being the surface density of adsorbed dipoles. The corresponding work function change is:

$$\triangle\, \phi = -qE_C d \tag{2.20}$$

where E_C is the electric field within the dipole layer.

In a more rigorous treatment it has to be taken into account that the electric field at the site of a particular dipole is modified by all the surrounding dipoles [47]. A depolarization effect occurs so that an effective electric field has to be added with a dipolarization factor [29]

$$f_{dep} = \frac{9\alpha n_{dip}^{3/2}}{4\pi\epsilon_0} \tag{2.21}$$

where α is the polarizability of the adsorbed particles. Thus the dipole-induced work function change can be obtained as

$$\triangle\, \phi = -\frac{e}{\epsilon_0} p\, n_{dip} \left(1 + \frac{9\alpha n_{dip}^{3/2}}{4\pi\epsilon_0}\right) \tag{2.22}$$

Since neither the dipole moment p nor the polarizability α of the adsorbed molecule are well known, it is difficult to apply (2.22) to real experiments.

Nevertheless, in a more qualitative picture two important contributions to the work function change can be considered

$$\triangle\, \phi = D_{chem} + \triangle D \tag{2.23}$$

1. D_{chem} comes from the formation of a chemisorption dipole between the metal and the adsorbate due to the charge transfer in chemisorption.

2. $\triangle D$ is due to the modification of the metal surface dipole upon adsorption. The presence of a molecule leads to a shortening of the electron density tail at the metal surface [31]. As a result the metal surface dipole is significantly reduced and the work function decreased by the same amount.

2.2.2 Acrylonitrile

Acrylonitrile (H_2C=CHCN) is a colorless, odorless and poisonous liquid. It is usually used for producing Acrylic Fibers, ABS/SAN Synthetic resin, Acrylamide, synthetic rubber and Latex. It also has applications in microelectronics as electrochemically thin films of the molecule can be deposited onto metallic substrates. 90% of the world production of around 5 million tons is based on the SOHIO process

$$C_3H_6 + O_2 \rightarrow C_2H_4CO + H_2O \tag{2.24}$$

$$C_3H_6 + 3/2O_2 + Nh_3 \rightarrow CH_2CHCN + 3H_20 \tag{2.25}$$

which has been developed in the late 50's by workers of the Standard Oil of Ohio Company. In the SOHIO process selective oxidation (2.24) and ammoxidation (2.25) lead to the production of acrelein and acrylonitrile. The overall process takes place in the vapor phase in the presence of a catalyst ($Bi_2O_3MoO_3$).

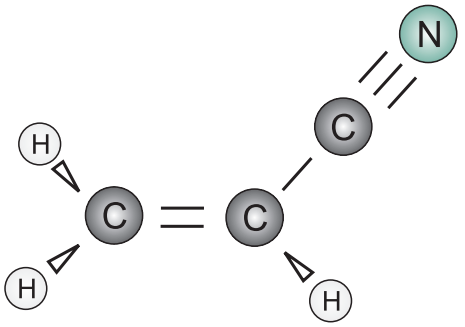

Figure 2.4: Acrylonitrile in gas phase.

Beside the industrial importance acrylonitrile has gained attention with the exploration of Jupiter's moon Titan. Its atmosphere is in some points comparable to the early earth's atmosphere (i.e. 1.5 bar pressure, high N_2-rate of around 90%), water and complex chemical products, like acetonitrile or cyanogen, have been detected. Since the temperature at the surface is around 93 K, chemical reactions should be photon-driven. Although acry-

lonitrile has not been detected yet, irradiation of mixtures of gases comparable to Titan's atmosphere suggest its formation as photoproduct in a nitrogen:cyanoacetylene mixture or in a photolysis of acetylene and hydrogen cyanide [32].

Symmetry	Mode	Nature of Mode	Wave number	Energy	Relative intensity[a]
A'	ν_1	C-H stretching	3125	387	S
	ν_2	C-H stretching	3078	382	S
	ν_3	C-H stretching	3042	377	S
	ν_4	C≡N stretching	2239	278	W
	ν_5	C=C stretching	1615	200	M
	ν_6	CH_2 deformation	1416	176	M
	ν_7	CH rocking	1282	159	W
	ν_8	CH_2 rocking	1096	136	W
	ν_{11}	C-C stretching	869	108	M
	ν_{13}	C=C-C bending	570[b]	71	
	ν_{15}	C-C≡N bending	242[b]	30	
A"	ν_9	CHR wagging	972	120	VS
	ν_{10}	CH_2=C wagging	954	118	VS
	ν_{12}	C=C torsion	683	85	S
	ν_{14}	C-C≡N wagging	954[b]	118	VS

Table 2.1: Symmetries, natures of modes, wave numbers (cm^{-1}), energies (meV) and relative intensities in the infrared gaseous spectroscopy for the fundamental vibrations of acrylonitrile, taken from [53]
[a] VS-very strong, S-strong, M-medium, W-weak
[b] The wave number of these vibrational modes are only given for the liquid phase

In the electronic ground state the acrylonitrile molecule is planar (fig. 2.4). It has 15 normal vibrational modes (shown in table 2.1) which are all both infrared and Raman active. Eleven vibrations are in the plane of the molecule and of the A' type (symmetric with respect to reflection of the molecular plane) whereas there are four vibrational motions out of the plane belonging to the A" (antisymmetric) irreducible representation.

2.2.3 Chemisorption of acrylonitrile on copper

While various geometries in the adsorption process of ACN on copper are possible experimental [33] and theoretical [34, 35] studies suggest two geometries as the most favorable (fig. 2.5):

1. ACN adsorbed flat on the surface. This corresponds to a very stable chemisorption via the C=C double bond and the nitrile group

2. ACN adsorbed perpendicular to the surface and bonded to the metal surface via the nitrogen lone pair.

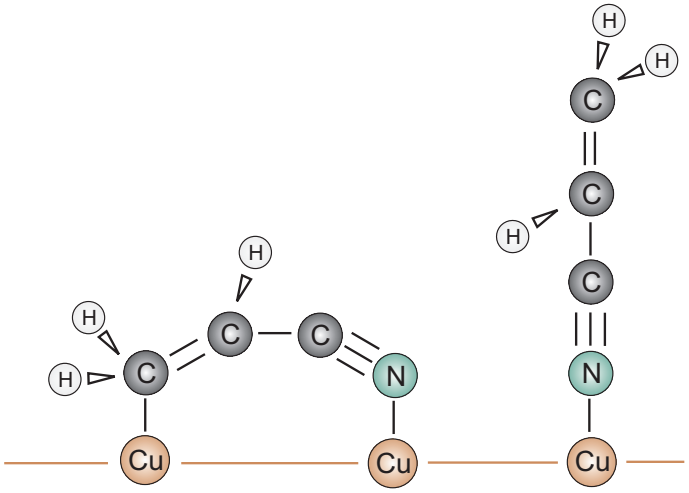

Figure 2.5: The two different geometries of ACN adsorbed on copper: di-σ adsorption via two terminal atoms, energetically more favorable, (left) and end-on σ-adsorption via the lone pair electrons on the N atom (right).

From the theoretical point of view DFT calculations show that the di-σ adsorption via the two terminal atoms (C and N) should be more likely due to the higher bonding energy ($E_b = 1.26$ eV), whereas the end-on σ-adsorption via the lone pair electrons on the N atom is less energetically favorable with a bounding energy of $E_b = 0.37$ eV, but still a stable configuration.

Experimentally, X-Ray photoemission spectroscopy (XPS) studies [33] show the presence of an ACN layer physisorbed on top of the a chemisorbed ACN mono-layer. The physisorbed ACN layer has a desorption temperature of around -145° C. Furthermore in thermal desorption XPS spectra two different types of chemisorbed ACN mono-layers can be observed. Thermal desorption experiments suggest that the mono-layer formed via ACN adsorption at -90° C is composed exclusively of molecules chemisorbed flat on the copper surface, whereas at lower temperature (-160° C) ACN molecules can be trapped in the less stable, perpendicular adsorption geometry.

2.2.4 Work function change by acrylonitrile

Considering the two contributions introduced in chapter 2.2.1 ACN is intermediate between the two extreme cases. XPS measurements [33] reveal that a partial electron charge transfer occurs from the metal surfaces towards the adsorbate. This chemisorption dipole is expected to increase the work function. UPS spectra reveal a decrease in the work function which indicates that

chemisorbed ACN strongly decreases the electric density tail of the metal and consequently the surface dipole of the metal, because the C and N nuclei are close (1.9 A) to the surface and the electron density of a metal surface is known to decrease exponential over several Angstroms [36].

Experimentally the work function change is observed by UPS to be $\triangle\phi = 0.5$ eV for an ACN monolayer on polycrystalline copper.

2.3 Resonances in electron scattering

Resonances in electron scattering is an electron-impact phenomenon, which involves the the formation of a transient atomic or molecular negative ion. The resonance electron scattering can be divided into a sequence of three events:

1. *Capture*: The process in which the incident electron is trapped by an affinity level of the molecule to form the negative ion-state.
2. *Dynamics*: The distortion of the intramolecular bonds (or electronic structure) of the host molecule during the lifetime of the resonance (typically 10^{-10} to 10^{-15} s). During this process the molecule is in an excited electronic configuration
3. *Detachment*: The process where the electron is eventually ejected from the negative-ion state

2.3.1 Vibrational resonances in electron scattering by molecules

Theoretical models for vibrational excitation are given by Gadzuk [37]. In this quantum-mechanical description the molecule is in a vibrational ground state of the neutral molecule $|\chi(t=0)\rangle$ at the time the electron attaches. The time required for the capture and emission of the incident electron is assumed to be much smaller than the vibrational period of the molecule.

According to the Born-Oppenheimer approximation [38], the vibrational and electronic degrees of freedom are separated, and the electronic state of the molecule determines the potential-energy surface on which intramolecular motion takes place. Whilst the electron remains trapped in the molecular ion, the molecular vibrational wave function evolves in time according to the Hamiltonian of the negative ion H_{ion} [37]

$$|\chi(t>0)\rangle = e^{-\frac{i}{\hbar}H_{ion}t}|\chi_0\rangle \tag{2.26}$$

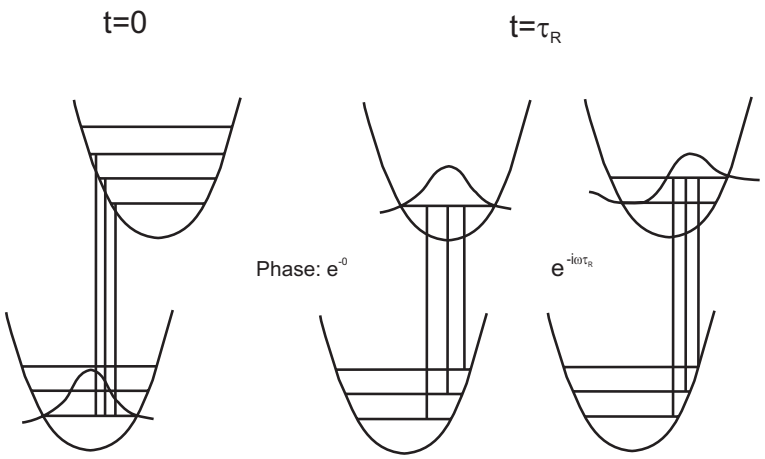

Figure 2.6: A schematic diagram of resonant vibrational excitation by displaced oscillator potentials of the neutral molecule and negative ion showing representative vibrational wave functions and phase factors acquired during the lifetime of the negative ion (Frank-Condon picture).

The detachment of the electron causes the molecule to make a sudden transition back to the potential-energy surface of the neutral molecule. After emission, the vibrational wave function of the molecule consists of a superposition of all the vibrational eigenstates of the neutral molecule, so that the probability of detecting the molecule in the n-th vibrational state is [39]

$$P_{0->n} = |\langle \chi_n | e^{-\frac{i}{\hbar} H_{ion} t} | \chi_0 \rangle|^2 \tag{2.27}$$

In a first approximation the energy and lifetime can be considered equal because the resonance width ($\sim 1/\tau$) is just the imaginary part of the complex resonance energy. But a number of factors perturb the energy and resonance lifetime on the surface. The influence of the image potential together with the perturbation of the molecular potential by the the bonding have to be considered.

2.4 Photochemistry of acrylonitrile on copper

In previous experiments [13, 14] the laser induced ACN dissociative attachment has been proven, in which furthermore a wavelength dependence in the CN^-/e^--ratio has been observed (fig 2.7). In the CN^-/e^- spectrum peaks at the wavelength of the wagging modes ($\nu_9, \nu_{10,14}$) could be observed, red shifted by around 20 cm^{-1} possibly due to the weakening of the molecular bond associated to the bond formation between the adsorbate and the metal surface. The wavelength dependence of the electron yield can not be explained by a gas-phase attachment mechanism and indicates an adsorbate-substrate interaction. Furthermore the process is very endothermic (energy-absorbing),

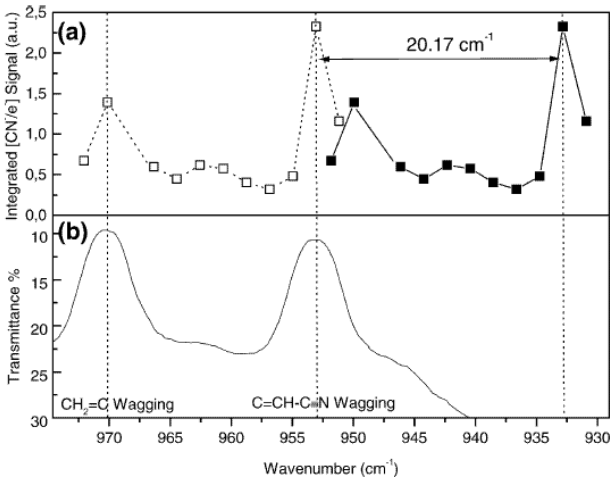

Figure 2.7: In the upper part an integrated electron yield obtained for ACN on copper irradiated with a CO_2-laser is shown. The filled boxes represent the CN^-/e^- ratio as a function of the laser wavelegth, the unfilled boxes the same as before but shifted 20.17 cm^{-1} to the blue part of the spectrum (a). For comparison the infrared gas-phase spectrum of ACN is given below (b).

so that for electron dissociative attachment electrons of at least 1.83 eV are necessary

$$\triangle H_0^O = D_0^O(A-CN) - EA(CN) = 5.66\,eV - 3.83\,eV = 1.83\,eV \qquad (2.28)$$

The surface reaction can take place by two mechanisms:

- *Substrate-mediated absorption.* The laser radiation heats the electrons in the substrate pumping them out of the Fermi level and subsequently they tunnel to the ACN^- potential which leads to A+CN^- products. This process is schematically shown in the left panel of fig. 2.8. Obviously, this mechanism would show a thermal character without significant frequency selectivity.

- *Adsorbate-mediated absorption.* In this case, the vibrational absorption of the ACN molecule is predominant. This may have several consequences: first an enhanced local heating of the surface electrons and therefore an enhanced realization of the first mechanism with the corresponding increase of the electron yield. Second, an increase in the CN^- yield due to a lowering of the DE value (fig. 2.8 right). Now the value of $\triangle E$ could be lower than $\triangle H_0^O$ since the ACN is adsorbed on the Cu surface and presumably the CH_2C-CN bond is softer and the resonant vibrational absorption increases the molecular electron affinity and so it facilitates the electron attachment.

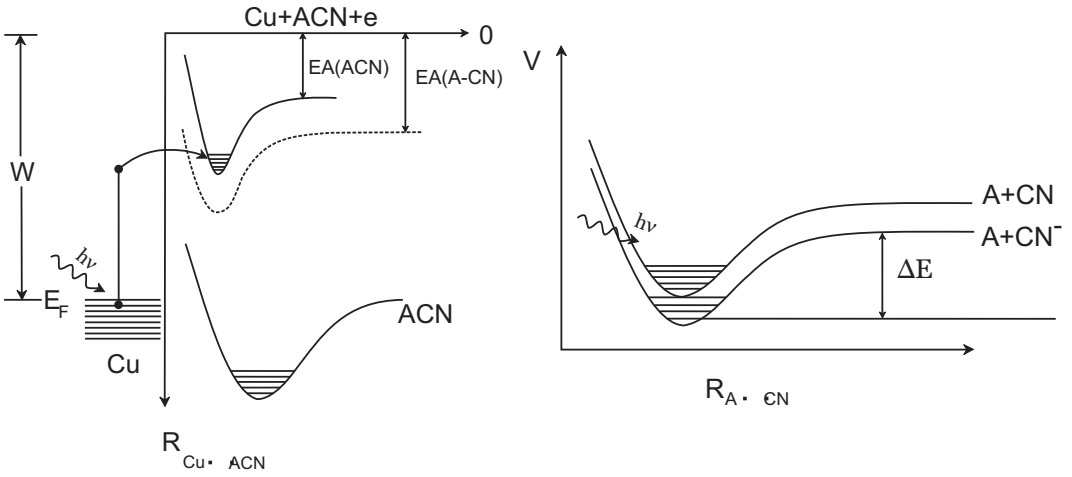

Figure 2.8: (left) idealized one-dimensional potential energy for the ACN/Cu system. Both neutral Cu..ACN and negative Cu..ACN$^-$ are displayed, W, E_F and EA stand for work function, Fermi energy and electron affinity, respectively. Dashed line represents the same Cu..ACN$^-$ potential but for an increased A..CN$^-$ distance so higher electron affinity at the asymptotic limit. The electron pumps out of the Fermi level and subsequent tunneling takes place. (right) neutral covalent and ionic A..CN potentials are qualitatively shown, in which the asymptotic energy difference is $\triangle E = D_0^0(A-CN) - EA(CN)$ (taken from [13] and modified).

Since the dissociative attachment of the adsorbed ACN also depends on its electron affinity, the observed enhancement in the CN^-/e^- ratio could be due to the lowering of the dissociative electron attachment barrier. In this picture, the ACN vibrational mode would function not only as an antenna for increasing the metal temperature, but it would also introduce some selectivity by reducing the surface reaction barrier due to the enhanced adsorbate electron affinity. The resonant excitation remains localized during the very fast dissociative attachment process such that subsequent energy transfer from the excited adsorbate into dissipative channels is not comparable to the rate of formation of the CN^- channel.

3. Experimental Setup

3.1 Experimental overview

The experimental system consists of a Ultra-High-Vacuum chamber, which is pumped by two turbomolecular pumps (Leybold TW300H 220 l/s, Pfeiffer-Balzers TPU 240H 200 l/s). A great care was taken in the selection of the stainless steel (AISI 310 and AISI 316L), the structure materials of the experiment table (aluminum profiles), as well as the rest of the materials to avoid additional stray magnetic fields.

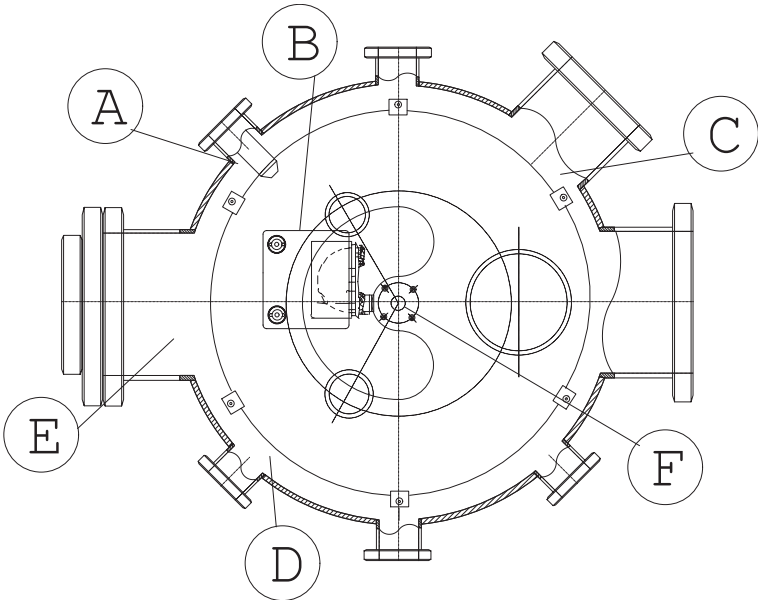

Figure 3.1: Upper view of the experimental setup. On the drawing appear some of the components of the system: Ion gun (A), hemispherical electron analyzer (B), Quadrupole (C), electron gun (D), Time of flight mass spectrometer (E), the sample is placed in (F).

An Argon-ion gun (Vacuum Generators AG5000) is installed in a 45 °angle for cleaning the surface by ion sputtering and a quadrupole mass spectrometer (VG SX300) has been applied for desorption experiments.

The electron pulse is analyzed with a hemispherical electron analyzer with dual microchannel plates (MCP) for electron detection, connected to a custom made sensitive charge preamplifier. The output of the preamplifier is connected to an amplifier (Stanford Research Systems, SR445) and an integrator boxcar(SRS, SR250). The voltage ramps for the spheres of the electron analyzer are created by high voltage power supply (CMTE 3103D) controlled by a function generator (Agilent, 33250A, 80 MHz). With this setup, ramps of millivolts can be created mounted on hundreds of volts. The integrated electron signal from the boxcar and the value of the ramp is monitored and digitized simultaneously in an oscilloscope (LeCroy, LC334AM, 500 MHz) with a time scale of tenth of seconds per ramp.

The electron emission is measured while varying automatically the wavelength of the OPO-laser controlled by an acquisition program designed for this purpose (Adquire).

3.1.1 Electron analyzer

As it was mentioned in the previous chapter, the electron signal is analyzed by a 180 degrees hemispherical electron analyzer. It is made of aluminum and consists basically of an inner sphere (R_1=16 mm), an outer sphere (R_2=34 mm), an Einzel lens and two microchannel plates (Topag MCP-MA25/2) like shown in figure 3.2.

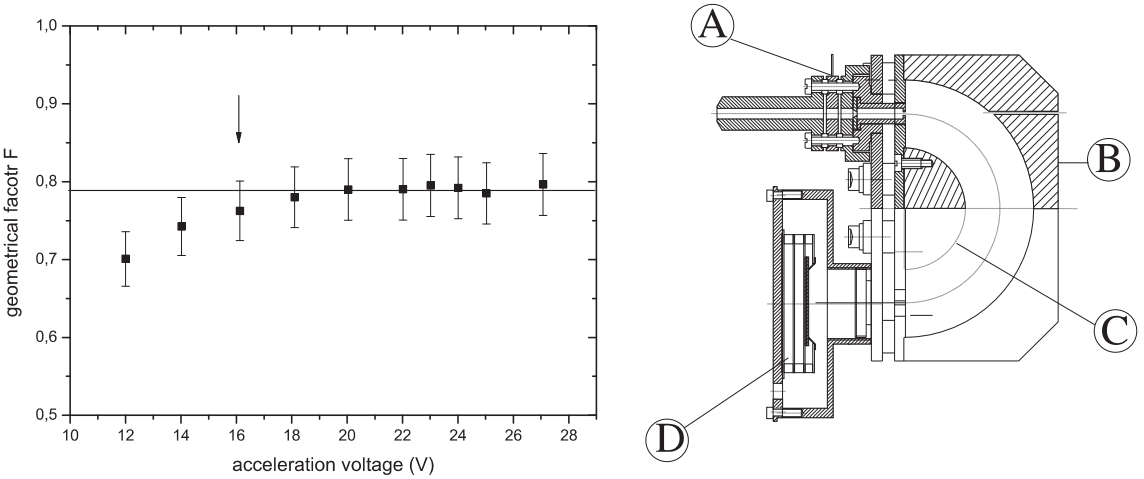

Figure 3.2: Results on the measurement of the geometrical factor on the left, the arrow indicates the starting point below which the influence of the magnetic fields is so high that it affects the measurements. The sketch of the electron analyzer on the right with its principal parts: einzel lens (A), the inner and outer spheres (B and C) and the microchannel plates (D).

To check the influence of stray fields in the electron signal, a small electron gun electrically isolated from the analyzer was installed in the entrance, so that the filament could be set on a certain voltage. At the exit we installed a Faraday cup [49] measuring the current at the anode with an electrometer (Keithley, 610CR). The energy of the electrons necessary to pass the analyzer can be written as [41]

$$E_0 = \frac{e \triangle V}{F} \tag{3.1}$$

where $\triangle V$ is the difference of voltage between the spheres and F the geometrical factor of the analyzer which is defined by

$$F = \frac{R_2}{R_1} - \frac{R_1}{R_2} \tag{3.2}$$

with a theoretical value of $F^{-1} = 0.605$. In figure 3.2 the experimental measurements for $1/F$ are shown in respect to the kinetic energy at the entrance of the analyzer. For electron energies above 16 eV the geometrical factor remains constant at $1/F = 0.788$, while it is decreasing for energies below 16 eV. At this energy the influence of the magnetic fields is so high that it affects the measurements and cannot be neglected.

3.1.2 Sample preparation

A real surface under atmospheric pressure is far from the ideal system desirable, since a clean surface is very reactive towards molecules impinging on it. Therefore repetitive cleaning cycles and UHV conditions ($< 10^{-9}$ Torr) are necessary to maintain a well defined surface. The ambient pressure and the sticking coefficient determine the time between two cleaning cycles.

The ambient pressure determines how many particles of the residual gas impinge on a surface area of 1 cm^2 per second through the relation

$$p = 2m\langle v \rangle \dot{z} \tag{3.3}$$

where m is the mass of the gas atoms, $\langle v \rangle$ their average thermal velocity and $\dot{z}$ the impinging rate [$cm^{-2}s^{-1}$]. Based on this formula a dosage unit can be defined: 1 Langmuir (1L) is the dosage corresponding to exposure of the surface for 1 s to a gas pressure of 10^{-6} Torr. For a sticking coefficient of unity the exposure of 1 L causes an adsorbate coverage of around one monolayer.

The standard cleaning method in surface science is by ion bombardment and annealing. The topmost layers of the crystal are sputtered off by bombardment with noble gas ions. After having removed all contaminants the surface is healed out by annealing up to 700 °C.

The sample ion bombardment was done with a commercial argon ion gun with a acceleration voltage up to 5 kV. Six cycles of 5 minutes sputtering and and 10 minutes heating were applied for first time cleaning of the sample, in daily working conditions one to three cycles were sufficient.

The sample heating was done by electron impact on the rear part of the sample. For this purpose a sample holder (Vacuum Generators mod. SH1) was modified. A small electron gun with Einzel lenses was designed and installed as can be seen in the Figure. The Einzel lenses allow to focus the electron beam in such way to spread the electron beam on the sample surface homogeneously. The hairpin shape of the W-Th (2%) filament allow us to work with the electron gun in a well defined pulsing mode. With this configuration we could heat the metallic sample for cleaning as well as a gentle heating with a precise control of the sample temperature during liquid nitrogen (LN2) cooling.

The filament was mounted on several hundreds of volts and delivered milliamperes with a pulse repetition of 1 kHz generated by square pulses from a function generator (Agilent Mod. 33250A 80MHz). The average electron current on the sample could be precisely measured with a electrometer (Keithley Mod. 610CR). In the future precise temperature control can be done by changing the duty cycle. For temperature control in the range of LN2 temperature the filament will be mounted only on several tenths of volts allowing temperature control of less than 0.1 K.

To measure the sample temperature a K-type thermocouple (NiCr/NiAl) is installed in thermal contact with the sample and the signal was amplified and filtered for data acquisition (Adlink DAQ-2501) with LabView acquisition programs (LabView 8.0).

3.1.3 Gas inlet system

To avoid the disadvantages of filling an ultra high vacuum system with gas in order to study adsorption processes a beam dosing system was designed and constructed. These disadvantages relate to the large gas loads needed for system dosing. Such large loads result in adsorption on the walls of the vacuum chamber, which then leads to a slow recovery of base pressure after adsorption by the sample surface is complete. In addition, large gas loads in a vacuum system can cause displacement effects from the system walls leading to impurity adsorption, as well as regurgitation effects from, for example, ion pumps or titanium sublimation pumps.

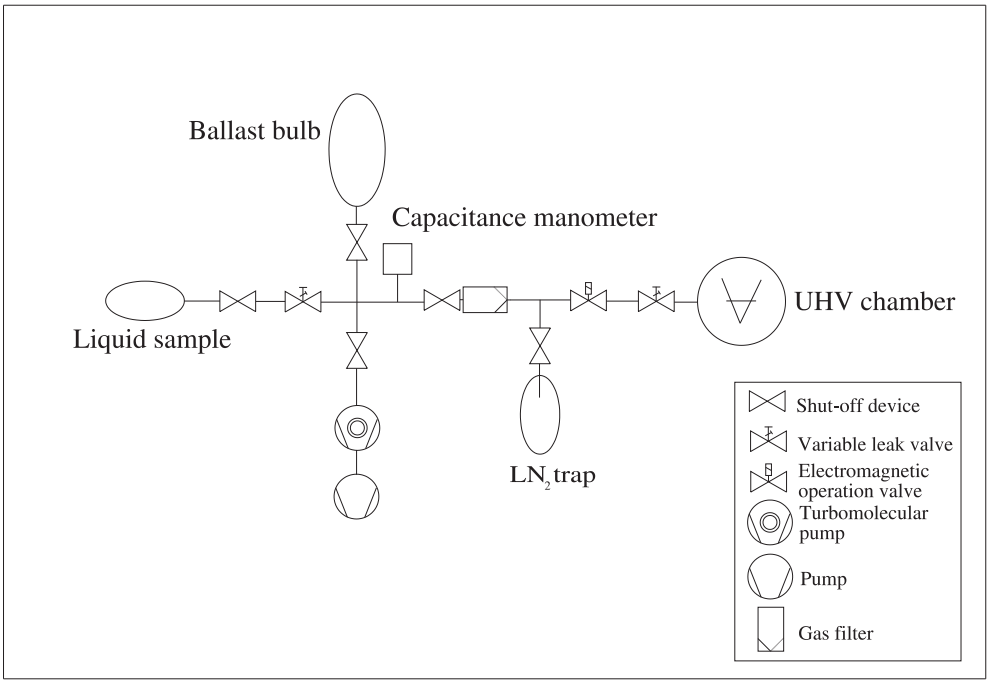

Figure 3.3: The gas inlet system.

There are different solutions for beam dosing: beam doser, a capilar and a pinhole. Although the beam doser and the capilar has the better performance than the pinhole, they were dismissed because of the well known isotopic exchange between the Si-OH groups of the glass-doser/capillar and the OD groups of the molecules of interest as D_2O. Thus a metallic pinhole with a diameter of 10 μm was selected.

The gas inlet system was made of stainless steel fittings of 1/2" (Parker Instrumentation, Swagelock and Cajon-VCR) and was pumped by a turbomolecular pump (Pfeiffer TPU-240). The stainless steel system could be baked with heating tape to 150-200°C while pumping with the turbopump. Because of the low pumping speed through the narrow tubing and the relatively high internal surface area compared to the volume, limiting pressures in the 10^{-7} mbar range were usually measured. For gases added to the mbar level this background gas represents less than 1 ppm of added impurity, which is usually less than the initial purity of the gas being studied.

To measure the pinhole conductance, a ballast bulb of exactly known volume was filled with an inert gas (N_2 for example) and following monitored by measuring the time rate of change of pressure in the ultrahigh vacuum chamber with a shielded quadrupole (Vacuum Generators SX-300). With this system very accurate and controlled expositions could be done.

3.2 Laser system and optical path

3.2.1 Nanosecond Laser

The laser system is a Q-switched Nd:YAG laser (Coherent Infinity) delivering pulses of temporal width of 3 ns and repetition rate between 0.1 and 30 Hz. The fundamental output of the Nd:YAG is 1064 nm at around 200 to 300 mJ. It is frequency tripled (355 nm) by two non-linear crystals and directed into an optical parametrical oscillator (OPO). The output power of the OPO is around 5 to 15 mJ, depending on the wavelength.

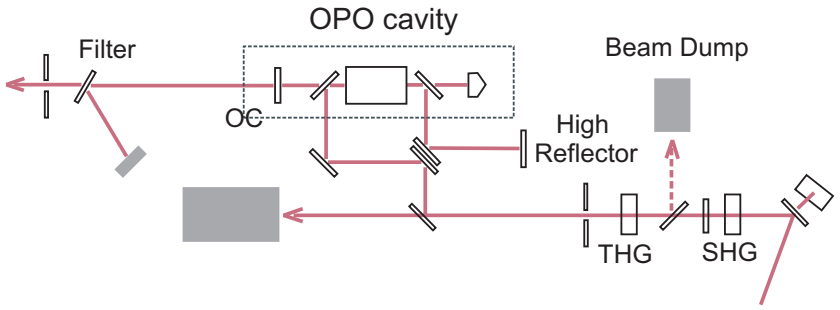

Figure 3.4: The OPO design: The incoming beam of 1064 nm, is frequency doubled (SHG) and after that frequency tripled (THG) to pump the OPO cavity at 355 nm. The OPO cavity consists of the crystal housing the Porro Prism and the output coupler (OC). The beam is retropumped into the cavity by the High reflector.

3.2.1.1 Nonlinear crystals

The frequency of the laser light can be changed by using the nonlinear response of an optical medium in high electric fields. This nonlinear effects can only appear in anisotropic media like crystals or liquid crystals. In the Infinity laser system Beta-Barium Borate (BBO) is used. BBO crystals posses very good properties for nonlinear frequency conversion from the ultraviolet to the mid-infrared. They have a large temperature tolerance, low absorption and a very high damage threshold.

For high electric fields the induced dipole moments are not only of first order (linear) so that the polarization (density of dipole moments) can be expanded to the powers of the electric field: [50]

$$\vec{P} = \epsilon_0(\chi_1\vec{E} + \chi_2\vec{E}^2 + \chi_3\vec{E}_3 + \ldots) \tag{3.4}$$

The process of second harmonic generation (SHG) is a two step process: A polarization wave at the second harmonic $2\omega_1$ is produced which has a phase velocity and wavelength in the medium which is determined by n_1 the index of refraction for the fundamental wave. In the second step the energy is transferred from the polarization wave to an electromagnetic wave of frequency $2\nu_1$.

The phase velocity and wavelength of this wave are determined by n_2, the index of refraction for the doubled frequency. For efficient energy transfer it is necessary that the waves remain in phase. The highest efficiency is obtained when the crystal length equals the coherence length l_c: [51]

$$l_c = \frac{\lambda_1}{4(n_2 - n_1)} \tag{3.5}$$

The natural birefringence of uni- or biaxial crystals can be used to minimize dispersion. These crystals have two refractive indices for different directions of propagation. While n_1 is independent from the angle of incidence, n_2 is highly angular dependent, so that phase matching can be achieved by turning the crystal.

The frequency tripling is achieved by directing the fundamental wave and the second harmonic into another nonlinear crystal in which the waves are mixed to produce the third harmonic.

3.2.1.2 Parametric oscillator

The parametric oscillator consists of a Type II BBO crystal which is pumped by the third harmonic of the Nd:YAG (354.7 nm). The pump provides gain for two other wavelengths, the *signal* and the *idler*. By convention, the signal wavelength is shorter than the idler and the relation between them is given by: [52]

$$\nu_{pump} = \nu_{signal} + \nu_{idler} \tag{3.6}$$

For proper synchronization the phases of all three waves have to matched using the birefringence of the crystal. The tuning of the outgoing wave results in a change of angular condition (fig. 3.5) and therefore in a phasematching for different pairs of signal and idler waves.

The Infinity XPO cavity has a bi-noncollinear cavity design with a Porro prism as an end mirror and a flat output coupler. The pump light is coupled into and out of the cavity via two intracavity dichroic mirrors and is retroreflected to repump the crystal. Singly resonant OPO's have non-critical resonated wave angular acceptance when pump, signal and idler are collinear aligned. Phasematching rapidly becomes angle-critical with increasing noncollinear angle, but this is not exploited in a flat-flat cavity. With the proper imaging in a cavity with bi-directional pumping, the acceptance angle can be made critical and thus much smaller.

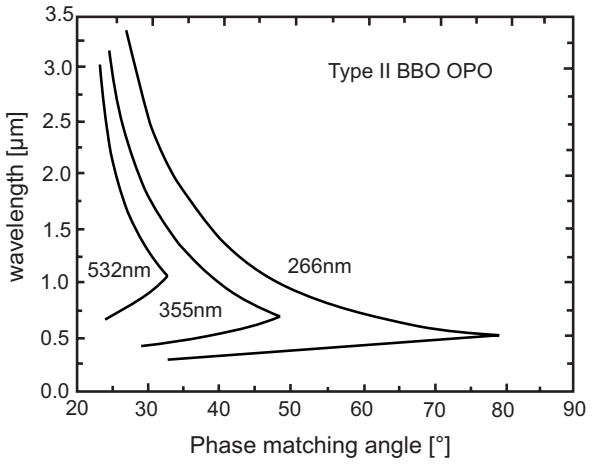

Figure 3.5: Phasematching curve for a type II BBO crystal for a parametric oscillator, taken from www.castech-us.com.

3.2.2 Optical path

At the exit of the laser the polarization is changed to p-polarization and the height is adjusted to the optical path by a periscope. Before entering the chamber the divergence is adapted by an galilean telescope and the energy adjusted by a variable attenuator (Newport M-935-5-OPT) down to 0.1 % of the incoming beam energy.

The optical path consists of several broad band mirrors (Thorlabs BB1-E02). Right before entering the chamber the beam is split to monitor the beam energy by a pyroelectric detector (Gentec ED-200A). The output power of the OPO is highly wavelength dependent and can vary up to 50% over the full range.

The angle of incidence of the laser beam with respect to the surface normal is 45° and is focussed with a achromatic lens with focal length of 300 mm. The spot size on the surface has been estimated to be around 1 mm. To minimize the effects of the surface heating, the incident power density was kept below 5 MW/cm^2. The maximum surface temperature rise with this power density and a 3 ns laser pulse can be estimated by using equation 2.9 to 11 K (fig. 3.6), so that the thermal effects can be neglected in the process of photoemission under the experimental conditions.

3.3 The TOF Mass Spectrometer

The construction of Time of Flight Mass Spectrometer (TOF-MS) has been published in 1946 by Stevens [40]. The principle is quite simple: ions of different m/z are dispersed in time during their flight along a field-free path of known length. Assuming all ions start their journey within a sufficiently

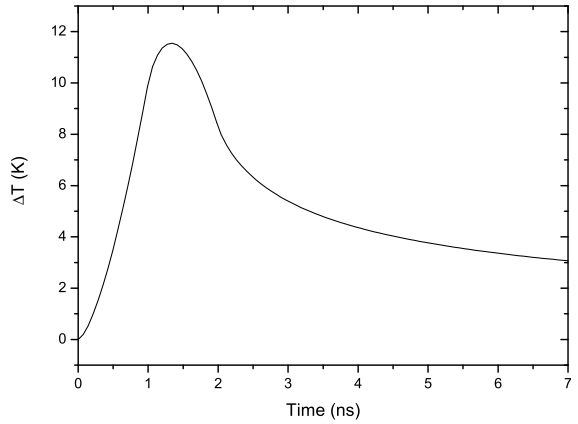

Figure 3.6: Increment of the local temperature for a 3 ns laser pulse.

short time interval, the lighter ones will arrive earlier at the detector than the heavier ones.

For this experiment a new TOF had to be designed for measuring the ions from photochemical processes at the surface. In the design of this TOF-MS the objective was not to reach the resolution of today's high resolution mass spectrometers rather than building a small but versatile instrument. Also the possibility of measuring the energy distribution of electrons should be given.

3.3.1 The design of the TOF-MS

The casing consists of Stainless Steel 316L and has a total length of 116 mm. The structure ending is conical to put the instrument as close to the surface as possible without interfering the laser beam. The grid at the entrance is fixed with a ring, which has a slightly larger diameter than the cone ending. At the beginning of the drift region an Einzel lens system is installed to focus the ions onto the detector since the diameter of the MCPs is only 20 mm. The lens apertures are made of aluminum and are separated from both the casing and each other by ceramic cylinders of 40 mm outer diameter and 32 mm inner diameter. At the housing of the MCPs a grid was installed and set to ground defining the end of the drift region.

The layout can be subdivided into three different regions, shown in figure 3.7. In the short source region, defined by the sample and the extraction grid, the ions are formed. A negative voltage (V) placed on the sample imposes an electric field across the field region, which accelerates all ions to the same kinetic energy:

$$\frac{mv^2}{2} = zeEs \tag{3.7}$$

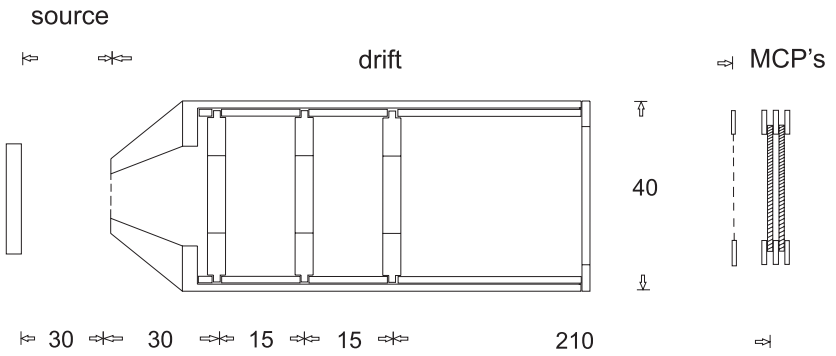

Figure 3.7: Design of the TOF-MS, extraction region, time of flight region and detector can be seen. All distances are in mm.

where s is the length of the source region. As the ions pass through the extraction grid they will have velocities inversely depending on the square root of there mass:

$$v = \sqrt{\frac{2eEs}{m}} \tag{3.8}$$

with $Es = V$, this equals a time of:

$$t_s = \frac{2s}{v} = 2s\sqrt{\frac{m}{2eV}} \tag{3.9}$$

After the source region, the ions pass through a much longer drift region (of length d). It is not completely field free since the middle aperture of the lens system is set to a negative voltage. Nevertheless ions gain no additional kinetic energy, because the outer apertures are set to ground so that the field is symmetric. The time of flight in this region will be:

$$t_d = d\sqrt{\frac{m}{2eV}} \tag{3.10}$$

In our case the last region, the detector region, is negligible, because the distance to the MCPs is around 10 mm and the potential difference 1000 V.

Due to the ionization process the ions will be formed in different locations, at different times, with different kinetic energies. This of course will influence their time of flight and their arrival time at the detector. The uncertainties in time of formation are rather small (3 ns) and maintain while the ions are traversing the TOF-MS. Since the surface is perpendicular to the electric field, the spatial uncertainties cannot result in a potential difference, so that uncertainties are rather given by the different trajectories, which result in slightly different times of flight. These effects can be simulated with SimIon.

More important are uncertainties in initial kinetic energy, which result in a different time of flight due to a different kinetic energy. This is a difficult term to correct when maximum mass resolution is needed, since increases in the drift length increase peak widths but also go along with the separation of peaks of different masses. The total time of flight of the ions can be calculated by

$$t_{tot} = \frac{s\sqrt{2m(U_0 + eV)}}{eV} + \frac{d\sqrt{2m}}{2\sqrt{U_0 + eV}} \tag{3.11}$$

3.3.2 Simulating the TOF-MS with SimIon

To have an idea about the properties of the TOF-MS various simulations have been done with SimIon7.0.

First simulations to determine the voltages that need to be applied for good angular acceptance revealed that setting the sample to -500 V is sufficient for detecting ions with up to 2 eV leaving the sample at 20° to the surface normal. The lens was set to -350 V. Since higher acceleration voltages lead to less mass resolution due to a limited time resolution, lowest acceleration voltage is favored with a high acceptance and reasonable resolution. The resolution simulated with these voltages is shown in figure 3.8 and is much higher than needed, since the peaks are separated by almost 10 ns (half maximum to half maximum). Ions of masses 26 (CN^-) and 27 were simulated with kinetic energies from 0-2 eV and up to 20° polar angle. The trajectories are shown in figure 3.9.The collection efficiency is 100 %.

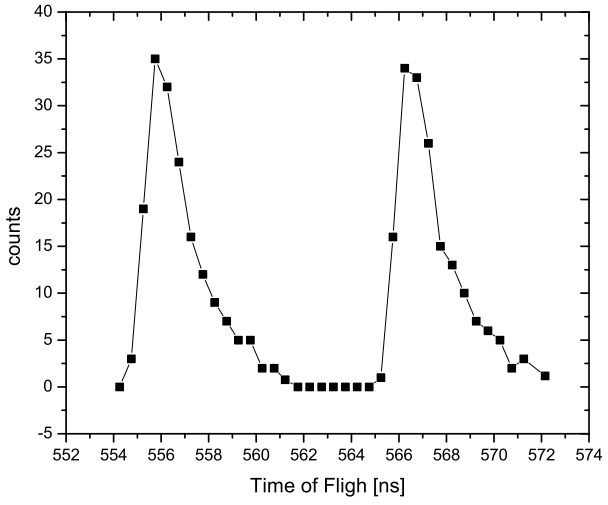

Figure 3.8: Simulation of the time of flight of ions of mass 26 and 27. From this graph it can be seen that the masses of the two peaks are clearly separated, so that ions in this mass regime can be identified.

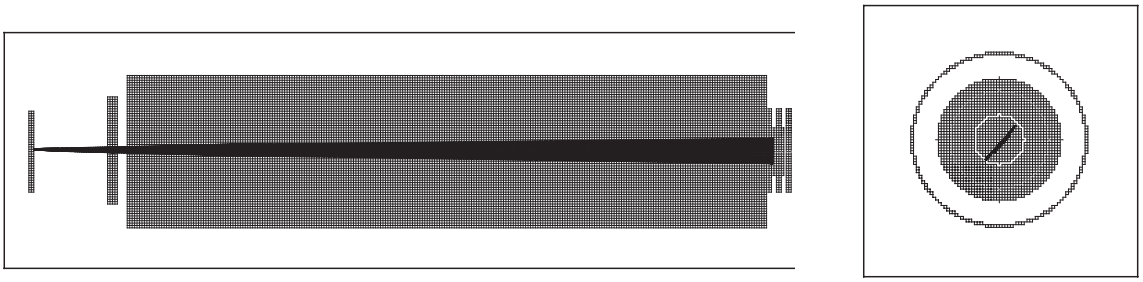

Figure 3.9: Simulation of the trajectories for ions leaving the sample with 2 eV and up to 20° in respect to the surface normal from the side (left). From the back view (right) it can be seen that all ions arrive within the detector area (inner circle).

In this setup also electrons are measured but due to the high acceleration voltages their energy distribution is compressed to one single peak. In applying lower acceleration voltages (20 V) and switching off the Einzel lens only electrons with a momentum in direction of the surface normal up to 5° polar angle are detected. The time of flight of the electron is around 100 ns (fig. 3.10).

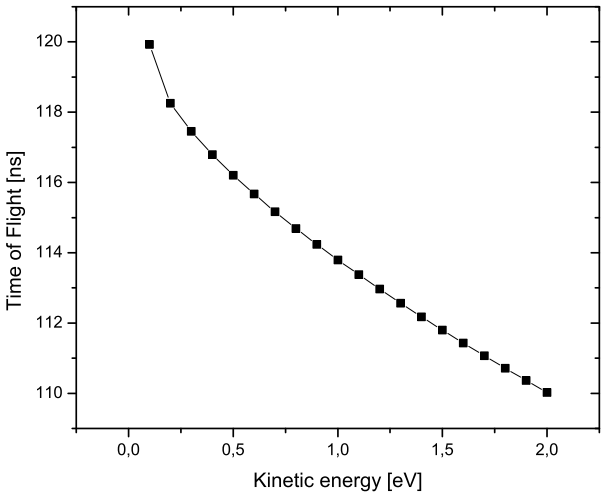

Figure 3.10: Simulation of the time of flight of electrons with different initial kinetic energy for 20 V acceleration voltage.

4. Results and discussion

4.1 Photoemission from copper

In the first experiment the existence of 2-Photon-Photoemission (2PPE) has been checked by measuring the electron yield against the power density of the laser (fig. 4.1). According to the theory of photoemission (chapter 2.1.3) the number of photons absorbed per pulse is given by the slope on logarithmic scale. It can be seen clearly that below 5 MW/cm^2 the slope is approx. two, indicating a 2PPE process. For higher power densities the emission has a big thermal component (Multiphotonemission).

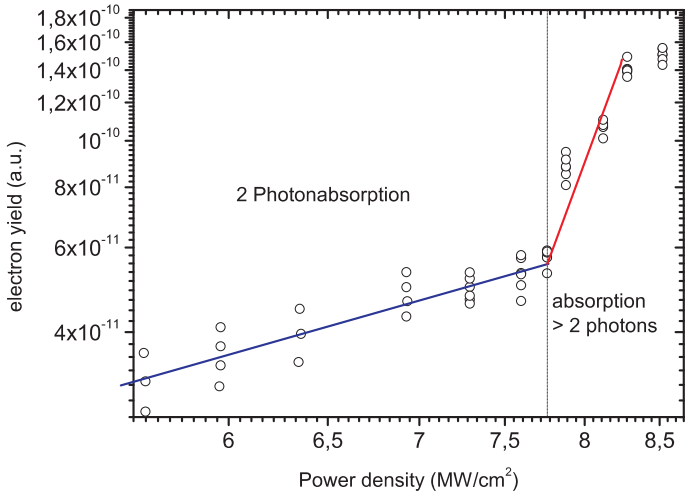

Figure 4.1: Check of the two photoemission, both axis are in logarithmic scale. For low power densities the emission follows a slope of two, indicating the 2PPE, for higher densities the emission is thermal.

As described in chapter 2.1.4 a strong dependence in the electron yield on the polarization of the incident light is expected. This has been observed in mea-

surements with 532 nm light turning a $\lambda/2$-plate changing the polarization in steps of 10 degrees. The electron yield along the surface normal shows a clear dependence on the polarization (fig. 4.2) of around one order of magnitude which is consistent with previous experiments. Therefore in the following experiments p-polarized light has been used to maximize the electron yield by smallest heating of the surface possible.

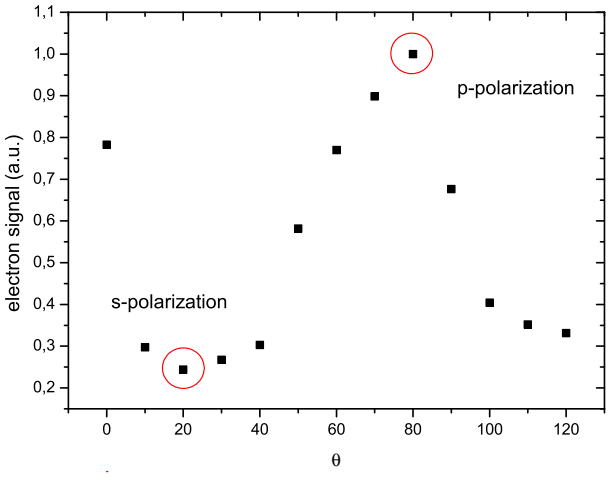

Figure 4.2: Electron yield dependence on the polarization of incident light is shown. Following theoretical predictions a difference of about one order of magnitude between s- and p-polarization can be observed.

In the next step a new experimental method has been developed to obtain the energy distribution of electrons with a selectable energy width generated by photoemission with a variable laser (OPO). Since the electron energy distribution broadens by decreasing the laser wavelength its width can be selected by varying the wavelength. In figure 4.3 the experimental results of photoemission from a polycrystalline copper surface are shown, which consist of the integration of 19 electron spectra generated by photons of energies between 2.07 eV and 2.49 eV. A dramatic change in the electron signal appears between 530 and 540 nm from which the work function of the polycrystalline copper can be deduced as 4.63 eV (while the tabulated value is 4.65 eV [42]. In figure 4.3(b) a normalized energy spectrum of the electrons corresponding to the integrated value in figure 4.3(a) signed by an arrow can be observed. The cutoff in the photoelectron spectrum is at about 100 meV, a little higher than the electrons should have by the absorption of 2 photons of 529 nm (76 meV). This can be due to two effects: the local heating effects or the absence of an adequate magnetic shielding. This last factor can be clearly seen in the spectrum of figure 4.3(b): the cut of the spectrum near 0 eV, reflects a resolution of 50 meV, while the nominal resolution of the analyzer should be 30 meV.

By lowering the range of the wavelength scan and increasing the number of scans to average, the precision in the measurement of the work function and the change under the presence of an adsorbate could be increased.

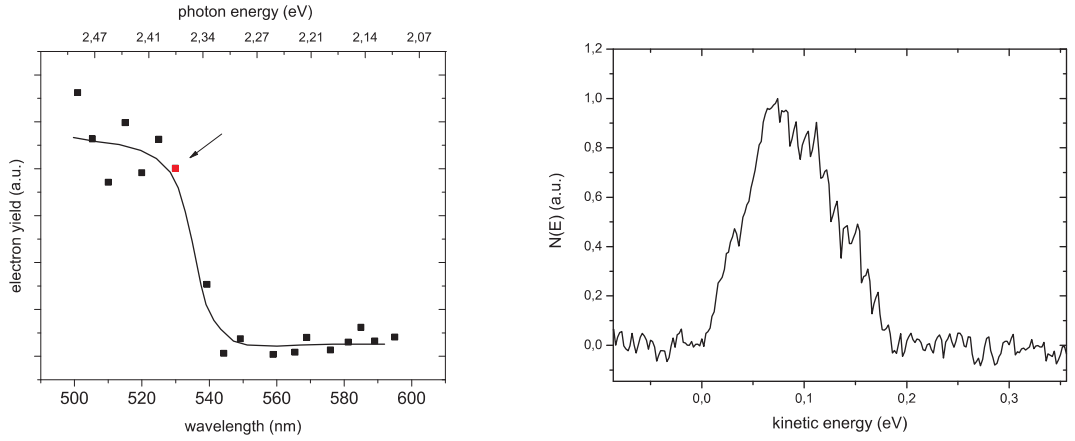

Figure 4.3: The integrated electron distribution against the incident laser wavelength is shown (left) and the correspondend electron signal to the point highlighted (right).

4.2 Photoemission from ACN covered copper

The copper surface was exposed to 2 and 5 Langmuir and the photoemission was generated with laser pulses of 2.34 eV and p-polarization.

The figure 4.4 (right) (note that the vertical scale is logarithmic) shows a photoemission spectrum for an exposure of 2 L. Similar results have been obtained for a 5 L exposition. Like in the results shown in section 4.1, electron signals below 30 meV were not detectable. A broader electron distribution than in the case of clean copper of energies up to 1.1 eV has been obtained. This result is consistent with UPS spectrum [33], which indicate a decrease in the work function of about 1 eV in the case of adsorption of ACN on copper. The value of the work function deduced from the photoelectron distribution is a little higher (approximately 150 meV) than the ones from UPS experiments due to: (i) the estimated resolution of the spectrometer is of some 100 meV at energies of 1 eV, so that higher precision measurements can not be presented, (ii) the higher energies of the photoelectrons can be produced by the heating of the sample which is not the case in the UPS spectra.

In figure 4.4 (left) an electron energy loss spectrum of ACN in gas phase is presented [43]. A remarkable increase in the band associated to the stretching of the C-H bond can be observed when the excitation energy is reduced (note that the spectrum for electron energies of 6.5 eV is amplified by the factor 80, whereas the 30 eV spectrum is amplified by 320)

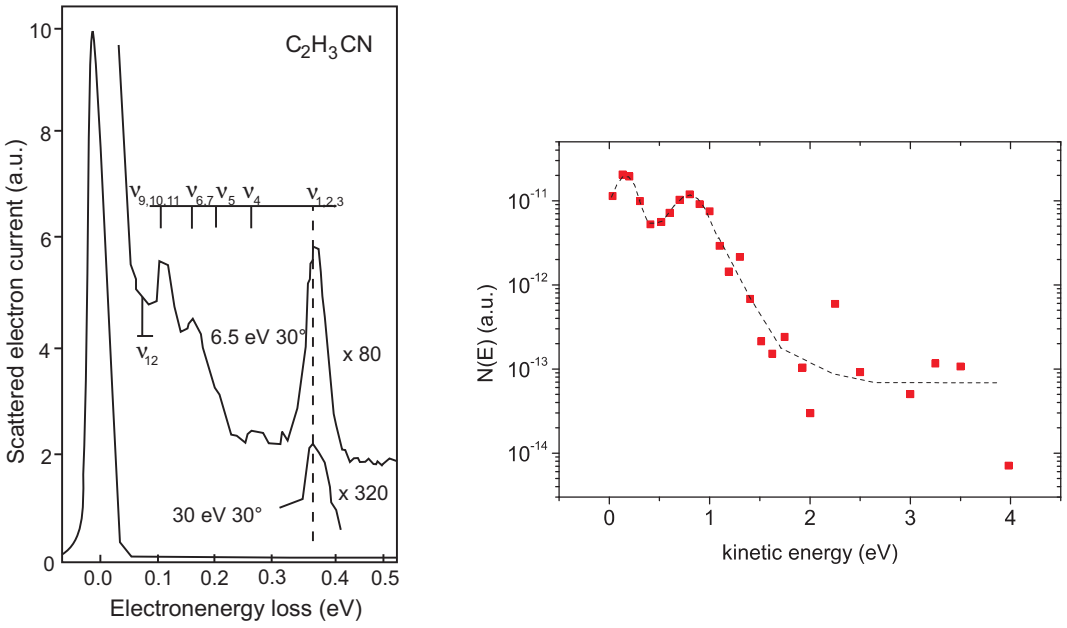

Figure 4.4: Electron energy loss spectrum of ACN in gase phase taken from reference [43] (left), photoemission spectrum of ACN adsorbed on copper (right).

Our measured electron spectrum shows a significant drop at 400 meV. The threshold energy for this channel should be lower than the value of the minimum location. In other words, only by proper deconvolution the onset for the stretching excitation can be determined. This should be lower than the experimentally "broadened" 400 meV. Possibly it corresponds to the excitation of the vibrational modes $\nu_{1,2,3}$ stretching the C-H bond of the ACN molecule. In gas phase the excitation energy of these modes is about 378 meV, a value which is consistent with our measurement taking into account the experimental error (the theoretical resolution of the spectrometer for these energies is about 30 meV).

It is interesting to point out that the increase of the $\nu_{1,2,3}$ band demonstrated in figure 4.4 (right) suggests the existence of a short-life resonance with excitation energies between 0 and 10 eV in gas phase. Figure 4.5 shows a magnification of the figure 4.4(b) between 0 and 2 eV. The maximum of the resonance can be observed, by deconvoluting a gaussian function from the photoemission spectrum, at 385 meV corresponding to the gas phase spectrum.

No negative ion from the ACN/Cu system or its fragments has been detected in this experiments, maybe because the electron energy was to low to open dissociation channels. In gas phase [44] for energies above 1.6 eV a dissociative channel opens with the creation of CN^-. In adsorbed phase the CN^- ions could be detected [13] and although the kinetic energies could not be measured, the electron energies were probably higher than the ones created in the present study.

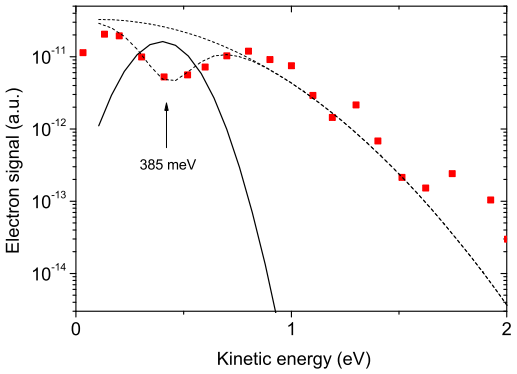

Figure 4.5: Photoemission spectrum of electrons from copper with ACN adsorbed for energies between 0 and 2 eV. The center of the drop in the electron signal can be observed at 385 meV.

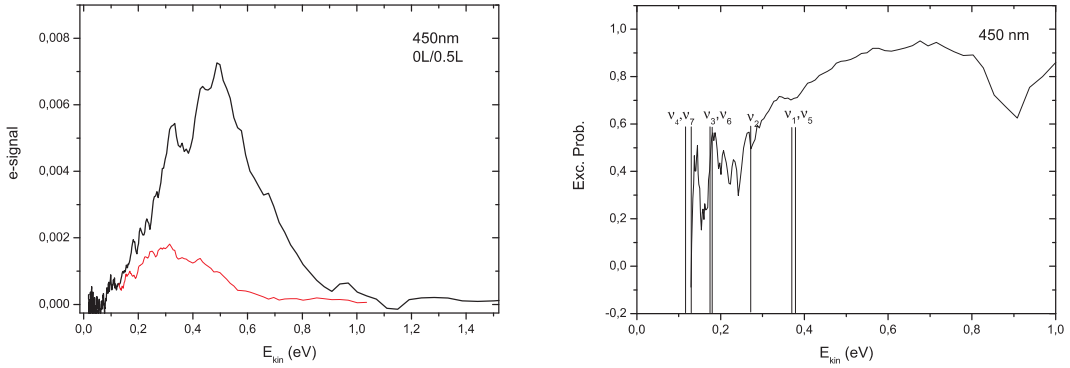

Figure 4.6: The electron signal in respect to the electron energy is shown at 450 nm incident light for clean copper (black) and with low exposure of 0.5 L ACN covered copper (red) on the left. A clear decrease in the electron signal can be observed. On the right the attenuation probability for the electrons and the energy of the vibrational excitations is shown.

Further experiments have been carried out by measuring the electron energy distribution using a TOF-MS. The TOS-MS technique give the possibility of decreasing the laser power density but maintaining the electron signal. The disadvantage is less energy resolution than the electron analyzer.

TOF-MS spectra were recorded with different laser wavelengths from 450 nm up to 490 nm under a 2-photon photoemission. For conversion time to energy the metallic sample was set to different voltages to obtain different time of flight spectra consistent with SimIon simulations.

Figure 4.6 (left) shows two electron energy distributions generated with 450 nm photons at the same laser power density. A broad (up to 0.9 eV) electron energy distribution is observed when no ACN is adsorbed on the surface (thick solid line). After a soft ACN exposition (0.5 L) the electron signal is smaller and the distribution is narrower (thin red line). Figure 4.6 (right) shows the

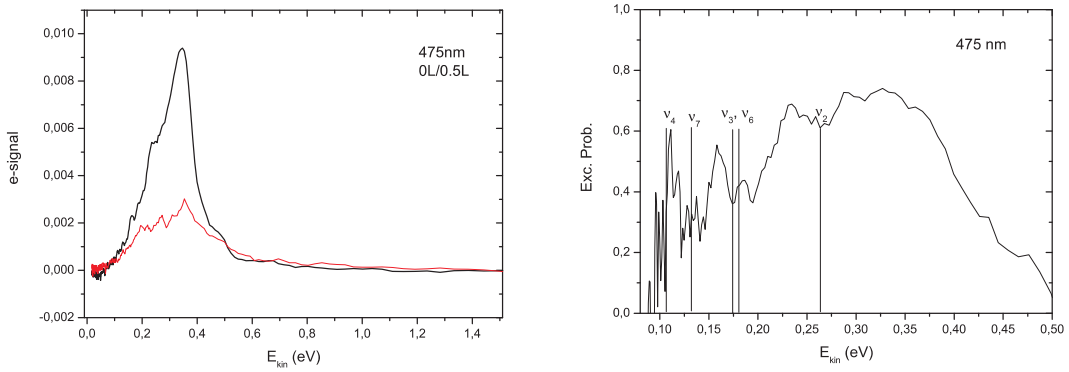

Figure 4.7: The electron signal in respect to the electron energy 475 nm incident light for clean copper (black) and with low exposure of 0.5 L ACN covered copper (red).

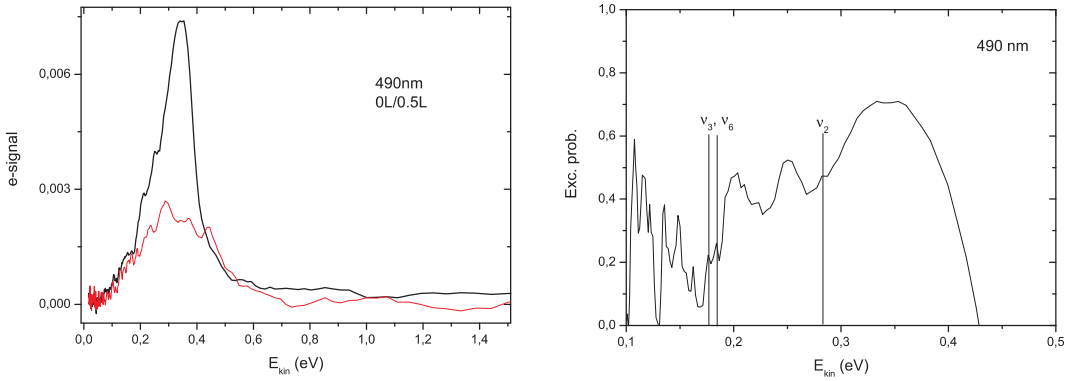

Figure 4.8: The electron signal in respect to the electron energy 490 nm incident light for clean copper (black) and with low exposure of 0.5 L ACN covered copper (red).

ratio between both distributions that will be named as attenuation probability and defined as:

$$Excprob = 1 - \frac{esignal_{0.5L}}{esignal_{0L}} \tag{4.1}$$

The vertical lines show the energy thresholds for the vibrational excitation of the ground state ACN molecule as labeled in table 2.1. As it is well known [39] the maximum of the mode excitation appears some meV above the threshold value. Several vibrational modes (from the highest energy one ν_1 down to the smallest compatible with the energy resolution on the TOF-MS ν_7 are excited when the broad energy electron distribution interacts with the adsorbed ACN molecules.

Figure 4.7 (left) shows both electron spectra generated with longer laser wavelength (475 nm) A narrower electron distribution could be recorded (thick solid line) obtaining electrons with kinetic energy up to 0.55 eV. With 0.5L of ACN the same vibrational modes where excited compared with 450 nm but

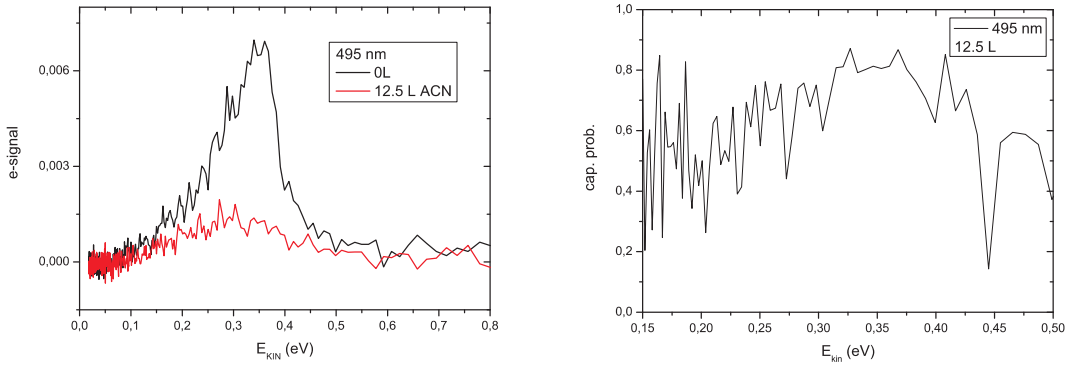

Figure 4.9: The electron signal in respect to the electron energy 495 nm incident light for clean copper (black) and with high exposure of 12.5 L ACN covered copper is shown (red). The much higher decrease in the electron than in the case of low exposition can be seen. The dependence of the attenuation probability on vibrational resonances is vanished.

in this case the ones with higher energy (ν_1 and ν_5) could not be resolved as a consequence of the low electron signal for these energies.

For low coverage the capture probability is significantly lower for electron energies below the excitation energies of vibrational modes. This is valid for all different photon energies in the figures 4.6-4.8. That means that for this low energy electrons (below 0.2 eV) the molecule is transparent independent on the laser wavelength. This situation changes with increasing coverage. For 12.5 L the coverage should be one monolayer or more, so that electrons can be multiple scattered back. Evidence can be seen in figure 4.9, where the attenuation probability is more or less constant for different electron energies.

5. Summary and Outlook

A new experimental system has been set up with the ability to investigate catalytic processes and charge transfer of acrylonitrile on copper. For this purpose a new Time of Flight Mass Spectrometer to measure both the reaction outcome and electron energy distributions has been designed and tested.

First experiments have been carried out, in which the width of the two-photon photoelectron energy distribution can be varied by changing the wavelength of the incident laser beam. This method allows high precision measurements of the work function and will be useful in the study with adsorbates, physi- or chemisorbed.

In first adsorption measurements the excitation of vibrational modes of acrylonitrile has been seen to be consistent with earlier gas-phase experiments. Electron energy spectra taken with the electron analyzer with high resolution showed a clear defect in the electron yield at energies around the energy of one vibrational mode, indicating the possibility of resonant vibrational excitation by electron impact.

More indications to that process were found i first electron spectra from the new TOF-MS, since a threshold for the capture probability is found at energies close to vibrational excitation. The threshold vanishes when the exposure is amplified significantly, indicating that electrons are scattered multiple and no resonance are be observed anymore.

The experiments carried out were just the starting point in understanding the mechanism of the reaction. A new femtosecond laser system which is currently set up will give not only a time-resolved information on the reaction pathways but also give the possibility to create non-thermal electrons and to

study intermediate states of the photoemission and the influence of the adsorbate on them. In addition the rotation of the electron analyzer will permit angle-resolved measurements of the scattering process of the electrons and the vibrational excitation via this pathway.

With the new cooling system applied it will also be interesting to study the excitation process at lower temperatures. Below -160°C there are different geometries of the molecule predicted to be present at the surface. At these temperatures the thermal effects should play a major role, so that a thermal decoupling of the electrons is very desirable.

Bibliography

[1] G.J. Schulz *Resonances in electron impact on atoms.* Rev. Mod. Phys. 45, 378 (1973)

[2] L. Sanche and M. Michaud *Resonance-Enhanced Vibrational Excitation in Electron Scattering from O2 Multilayer Films.* Phys. Rev. Lett. 47, 1008 (1981)

[3] E. Illenberger and P.Swidarek *Electron-driven molecular processes: A general introduction.* Eur. Phys. J. D 35, 173 (2005)

[4] R. Balog, M. Stano, P. Limão-Vieira, C. König, I. Bald, N. Mason and E. Illenberger *Low Energy Electron Interaction with Free and Bound SF_5CF_3 Negative Ion Formation from Single Molecules, Clusters and Nanofilms.* J. Chem. Phys. 119, 10396 (2003)

[5] T.H. Maiman *Stimulated Radiation in Ruby.* Nature 187, 493 (1960)

[6] J.F. Ready *Mechanism of Electron Emission Produced by a Giant -Pulse Laser.* Phys. Rev. 137, A620 (1965)

[7] R.W. Schoenlein, W.Z. Lin and J.G. Fujimoto *Femtosecond Studies of Nonequilibrium Electronic Processes in Metals.* Phys. Rev. Lett. 16, 1680 (1987)

[8] E.M. Logothetis and P.L. Hartman *Laser-Induced Electron Emission from Solids: Many-Photon Photoelectric Effects and Thermionic Emission.* Phys. Rev. 187, 460 (1969)

[9] M. Bonn, S. Funk, Ch. Hess, D. N. Denzler, C. Stampfl, M. Scheffler, M. Wolf and G. Ertl *Phonon- Versus Electron-Mediated Desorption and Oxidation of CO on Ru(0001).* Science 285, 1042 (1999)

[10] S. Daliwala, R.J. Finley, J.R. Goldman, T.H. Her, W.D. Mieher and E.Mazur *Surface femtochemistry of O_2 and CO on Pt(111).* Chem. Phys. Lett. 242, 617 (1995)

[11] M.E. Umstead and M.C. Lin *Effect of Laser Radiation on the Catalytic Decomposition of Formic Acid on Platinum.* J. Phys. Chem. 82, 2047 (1978)

[12] I. Her, R.J. Finlay, C. Wu, E. Mazur *Surface femtochemistry of CO/O_2 /Pt(111): The importance of nonthermalized substrate electrons.* J. Chem. Phys.108, 8595 (1998)

[13] J. O. Cáceres, J. Tornero y A. González Ureña. *Laser Catalysis of Acrylonitrile on Copper Surfaces.* Chem. Phys. Lett. 321, 349 (2000)

[14] J. O. Cáceres, J. Tornero and A. González Ureña. *Experimental Evidence of Vibrational Selectivity in Surface Charge-Transfer Reactions.* Surface Science 482-485, 562 (2001)

[15] H.Hertz *Über den Einfluss des ultravioletten Lichtes auf die elektrische Entladung.* Ann. Physik 31, 983 (1887)

[16] A. Einstein, *Über einen die Erzeugung und Verwandlung von Licht bereffenden heuristischen Gesichtspunkt.* Ann. Physik 17, 132 (1995)

[17] S. Hüfner *Photoelectron spectroscopy: principles and applications*, Springer , Berlin, 1995

[18] C.N. Berglund and W.E. Spicer *Photoemission Studies of Copper and Silver: Theory*, Phys. Rev. 136, A1030 (1964)

[19] J. B. Pendry *Theory of Photoemission* Surf. Science, 57, 679 (1976)

[20] M. Henzler, W. Göpel, *Oberflächenphysik des Feskörpers.* B.G. Teubner, Stuttgart, 1991

[21] G.L. Eesley, *Observation of Nonequilibrium Electron Heating in Copper.* Phys. Rev. Lett., 51, 2140 (1983)

[22] D. Burguess Jr., P.C. Stair y E. Weitz. *Calculations of the Surface Temperature Rise and Desorption Temperature in Laser-Induced Thermal Desorption.* J. Vac. Sci. Technol. A, 4, 1362 (1986)

[23] R.H. Fowler, *The analysis of photoelectric sensitivity curves for clean metals at various temperatures.* Phys. Rev. 38, 45 (1931)

[24] Lee A. DuBridge, *Theory of the Energy Distribution of Photoelectrons.* Phys. Rev. 43, 727 (1933)

[25] J.H. Bechtel, W. Lee Smith and N. Bloembergen *Two-photon photoemission from metals induced by picosecond laser pulses.* Phys. Rev. B 15, 4557 (1977)

[26] E. Hasselbrink, S. Jakubith, S. Nettesheim, M. Wolf, A. Cassuto and G. Ertl *Cross sections and NO product state distributions resultinfg from substrate mediated photodissociation of NO_2 adsorbed on Pd(111).* J. Chem. Phys. 92, 3154 (1990)

[27] A. Damascelli, G. Gabetta, A. Lumachi, L. Fini and L. Parmigiani *Multiphoton electron emission from Cu and W: An angle-resolved study.* Phys. Rev. B 54, 6031 (1996)

[28] H. Lüth, *Surfaces and Interfaces of Solids.* Springer Verlag, Berlin, 1993

[29] J. Topping, Proc. R. Soc. London A 114, 67 (1927)

[30] T.B. Grimley, *Theory of Chemisorption.* in: The Chemical Physics of Solid Surfaces and Heterogeneous Catalysis, Vol. 2, ed. by D.A. King, D.P. Woodruff, Elserevier, Amsterdam, 1983

[31] D.L. Price and J.W. Halley, *Electronic structure of metal-electrolyte surfaces: Three-dimensional calculation.* Phys. Rev. B 38, 9357 (1988)

[32] B.N. Tran, J.C. Jospeh, M. Force, R.G. Briggs, V. Vuitton and J.P. Ferris, *Photochemical processes on Titan: Irradiation of mixtures of gases that simulate Titan's atmoshpere.* Iracus 177, 106 (2005)

[33] X. Crispin, R. Lazzaroni, A. Crispin, V.M. Geskin, J.L. Brédas y W.R. Salanek. *Understanding the Initial Stages of Polymer Grafting on Metals: a Photoelectron Spectroscopy Study of Acrylonitrile Adsorption on Transition Metal Surfaces.* Journal of Electron Spectrometry and Related Phenomena, 121, 57 (2001)

[34] X. Crispin, C. Bereau, V.M. Geskin, R. Lazzaroni, W.R. Salaneck and J.L. Brédas, *Chemisorption of acrylonitrile on the Cu(100) surface: A local density functional study.* J. Chem. Phys, 111, 3237 (1999)

[35] V.M. Geskin, R. Lazzaroni, M. Mertens, L. Jérôme and J.L. Brédas, *Acrylonitrile on Cu(100): A density functional theoretical study of adsorption and electrochemical grafting.* J. Chem. Phys. 105, 3278 (1996)

[36] N.D. Lang and W. Kohn, *Theory of Metal Surfaces: Induced Surface Charge and Image Potential.* Phys. Rev. B. 7, 3541 (1973)

[37] J.W.Gadzuk in *Vibritional Spectroscopy of Molecules on Surfaces.* edited by J.T. Yates, Jr. and T.E. Madey, Plenum, New York (1987), p.45

[38] M. Born and R.Oppenheimer, *Zur Quantentheorie der Molekeln.* Ann. Phys. 84, 457 (1927)

[39] R.E. Palmer and P.J. Rous, *Resonances in electron scattering by molecules on surfaces.* Rev. Mod. Phys. 64, 383 (1992)

[40] W.E. Stephens: *A Pulsed Mass Spectrometer with Time Disperson.* Phys. Rev. 69, 691 (1946)

[41] *Electron Spectroscopy for Surface Analysis.* H. Ibach editor. Springer- Verlag, New York 1977.

[42] *CRC Handbook of Chemistry and Physics.* Edition 74, D.R. Linde (Ed.) CRC Press, Boca Raton, FL 1993.

[43] F. Motte-Tollet, D. Messina and M.-J. Hubin-Franskin, *Electronic and vibrational excitation of acrylonitrile by low and intermediate energy electrons.* J. Chem. Phys. 103, 80 (1995)

[44] M. Heni and E. Illenberger. *Electron Attachment by Saturated Nitriles, Acrylonitrile (C_2H_3CN) and Benzonitrile (C_6H_5CN).* Int. J. Mass Spec. and Ion Proc. 73, 127 (1986)

[45] I. Langmuir, *The constitution of fundamental properties of solids and liquids.* J. Am. Chem. Soc. 38, 2221 (1916)

[46] A. Zangwill, *Physics at surfaces.* Cambridge University Press, Cambridge, 1988

[47] E.P. Gyftopoulos and J.D. Levine, *Work function variation of metals coated by metallic films.* J. Appl. Phys. 33, 67 (1962)

[48] J.W. Gadzuk, *Resonant vibrational excitation in electron-energy-loss spectroscopy of adsorbed molecules.* Phys. Rev. B 31, 6789 (1985)

[49] W.R. Miller Jr and N.N. Axelrod. Rev. Sci. Instrum 37, 1096 (1966)

[50] J. Eichler and H.J. Eichler, *Laser.* Springer Verlag, Berlin 2003

[51] W. Koechner, *Solid-State Laser Engineering.* Springer Verlag, Berlin 1996

[52] *Operator's Manual of the Coherent XPO Laser.* Coherent, Santa Clara

[53] F. Halverson, R.F. Stamm and J.J. Whalen *The Vibrational Spectrum and Thermodynamic Functions of Acryloonitrile.* J. Chem. Phys. 16, 808 (1948)

[54] G.J. Schulz *Resonances in Electron Impact on Diatomic Molecules.* Rev. Mod. Phys. 45, 423 (1973)

Acknowledgements

Zunächst möchte ich mich bei Horst Schmidt-Böcking und Reinhard Dörner bedanken, dafür dass sie mich in der Gruppe aufgenommen und mir die Durchführung der Diplomarbeit ermöglicht haben. Horst's Kontakte sind ja bereits legendär, das dürfte wieder einmal eine Bestätigung dafür sein. Reinhard, vielen Dank auch für die Betreuung einer Arbeit die auf den ersten Blick nicht viel mit dem hier in Frankfurt zu tun hatte und vor allen Dingen für die materielle Unterstützung in Madrid.

I want to gratefully thank Angel Gonzales Ureña for the warm reception to his group in Madrid, the supervision of my diploma work and the support in Madrid.

Thank you to Gustavo Garcia for helping us with the experiment and fruitful discussions.

Furthermore I want to thank all the group in Madrid, especially Montse, Cristina and Arrantxa for a great time, Jorgito for sharing a room, Pepe and Stefan for their support and Segundo for mechanising all the pieces.

Thanks to my good friend Oscar for a really great time and a completely crazy trip to Javea. Thanks to all my flat mates in Madrid, especially Mirja, Valeska and Chaz.

Very special thanks to Beatrice and Sylvia for the good time, extraordinary hospitality and for all the support. I wish you all the best for your big project!

Thank you Jesús(senior) and your wife also for extraordinary hospitality, for a lot of help with the experiment and for introducing me to the real Spanish food.

Natürlich möchte ich auch der Gruppe hier in Frankfurt danken, die mich hier wieder hervorragend aufgenommen hat und mir die Rückkehr leicht gemacht hat. Danke Tim und Stefan fürs Korrekturlesen.

Ein riesigen Dank an alle, die mit mir durch dieses Studium gegangen sind, ohne euch hätte ich das wohl nicht geschafft, ganz sicher wäre es aber nicht so

lustig gewesen: Tim, Karo, Sven, Dominik, Dominique, Irina, Birte, Nadine, Kathi, Sportsfreund Peter, Jan, Bernd und Christoph.

Ganz besonders möchte ihr hier meinen engsten Freunden danken, die mich mal immer wieder in die Realität (bzw. zur Eintracht) zurückholen, danke Karo, Christoph, Patrick und Daniel "Son".

Natürlich geht der größte Dank hier an meine Familie. Meine Omas, meine Eltern und an mein Bruderherz, die mich mit allem was ich gemacht habe immer bedingungslos unterstützt haben und es mir ermöglichten, dieses Studium so durchzuführen, wie ich wollte, vor allen Dingen diesen Auslandsaufenthalt.

My biggest thanks in Madrid of course go to Jesús. You have been a really good friend (my Spanish girlfriend as Dani says) and a really good teacher. Thank you for a good time, in the lab with a lot of fun ("This is a disco") and a lot of hard work, and a good time outside the lab.

Ein ganz spezieller Dank geht natürlich an dich Dani. Danke für alles!

Zusammenfassung

In den letzten Jahren haben molekulare Prozesse in denen Kollisionen von niederenenergetischen Elektronen mit Adsorbaten oder gasförmigen Molekülen untersucht wurden gesteigerte Aufmerksamkeit auch durch verschiedene europäische Forschungsnetzwerke erhalten. Das Ziel ist die Kontrolle der Reaktionen, in denen niederenergetische freie Elektronen, Tunnelelektronen oder Photoelektronen aus Oberflächen eine Schlüsselrolle entweder bei der Aktivierung der Reaktion oder bei der Steuerung in bestimmte Reaktionkanäle spielen.

Diese Selektivität der Reaktionen erhielt mit dem Erscheinen der ersten Femtosekundenlasersysteme zusätzlichen Auftrieb. Nicht nur da sich die Reaktionen auf der Zeitskala von Femtosekunden abspielen, sondern auch da es erstmals gelang, die Photoelektronen thermisch vom Gitter zu isolieren. Die emittierten Elektronen sind nicht mehr im thermischen Gleichgewicht mit der Oberfläche, wodurch sich Reaktionen von Adsorbaten andere Kanäle öffnen.

Allerdings ist nicht unbedingt ein Femtosekundenlaser notwendig, um selektive Chemie an Oberflächen zu beobachten. In früheren Experimenten dieser Gruppe [13, 14] im Instituto Pluridisciplinar in Madrid wurde eine katalytische Reaktion von Acrylnitril (C_3H_3N) an einer polykristallinen Kupferoberfläche beobachtet, in der die Ausbeute eines Reaktionsproduktes (CN^-) abhängig von der Wellenlänge des eingestrahlten Lichtes war. Die dabei benutzte Lichtquelle war ein CO_2-Laser mit einer Pulslänge von 100 Nanosekunden.

Um den Mechanismus des Elektroneneinfangs und der vibrationalen Anregung des Moleküls genauer zu untersuchen, wurde dort ein neues System aufgebaut, das neben kürzeren Laserpulsen (3 ns) und einem anderen spektralen Bereich (450-650 nm) auch ein neues Detektorsystem besitzt. Zur Verfügung stand dabei ein hemisphärischer Elektronenanalysator mit einer Energieauflösung von 30 meV.

Thema dieser Arbeit war die Entwicklung eines Flugzeitmassenspektrometers, das neben der Bestimmung der Reaktionsprodukte auch eine grobe Energieauflösung der Elektronen gibt. Dies ist für erste Experimente interessant, da die Elektronenausbeute sehr viel höher ist als beim Elektronenanalysator, allerdings auf Kosten der Energieauflösung.

Die ersten Experimente, die mit diesem System gemacht wurden, dienten zur Bestimmung der Austrittsarbeit von polykristallinem Kupfer. Dabei wurde eine neue Art in der Messung eingeführt, in der die Wellenlänge des einfallenden Lichts kontinuierlich durchgestimmt wird. Die Energie pro Photon liegt im verwendeten Wellenlängenbereich zwischen 2 eV und 2,6 eV, so dass die Elektronen für die Überwindung der Potentialbarriere (ca. 4,6 eV) zwei Photonen absorbieren müssen. Da dies ein nichtlinearer Prozess ist, erhöht sich die Genauigkeit, so dass eine sehr genaue Bestimmung möglich ist. Die hierbei gewonnenen Ergebnisse von 4,63 eV sind in sehr guter Übereinstimmung mit den früher veröffentlichen Werten von 4,65 eV.

Weitere Experimente mit dem adsorbierten Molekül auf der Oberfläche wurden sowohl mit dem Elektronenanalysator als auch mit dem Flugzeitspektrometer durchgeführt. Bei den Messungen mit dem Elektronenanalysator wurde ein deutlicher Einbruch in der Elektronenausbeute bei der Energie in der Nähe der Anregungsenergie einer Schwingungsmode (Streckung der C-H Bindung) in der Gasphase gefunden. Dies deutet auf eine resonante Schwingungsanregung des Moleküls an der Oberfläche hin. Diese Vermutung wird unterstützt von Ergebnissen mit dem Flugzeitspektrometer, bei denen die Wellenlänge variiert wurde, so dass Elektronen mit höhere Energie erzeugt wurden. Bei geringer Bedeckung der Oberfläche erkennt man eine Schwelle in der Elektronenenergie unterhalb der keine Elektronen eingefangen werden. Die Wahrscheinlichkeit für Elektroneneinfang erhöht sich jeweils bei den Energien der Schwingungsanregung. Diesen Effekt kann man bei einer sehr hohen Bedeckung der Oberfläche nicht beobachten, die Einfangwahscheinlichkeit ist konstant hoch, was die Vermutung nahe legt, dass die Elektronen durch Vielfachstreuung an den Molekülen am Austritt gehindert werden.

Weitere Messungen in der Zukunft mit einem Femtosekundenlasersystem sind geplant. Dabei wird die Möglichkeit bestehen, die resonante Anregung zeitaufgelöst zu untersuchen. Desweiteren ist die Erzeugung von nichtthermischen Elektronen möglich, so dass eine vollständige Entkopplung der Reaktion von thermischen Effekten an der Oberfläche möglich sein kann. Bei den vorliegenden Messungen waren diese bereits sehr gering (11 K), sie kön-

nten aber eine größere Rolle spielen, wenn die Probe abgekühlt und damit in der Nähe der Temperatur kommt, an welcher verschiedene Orientierungen des Moleküls an der Oberfläche möglich sind (-160°C).